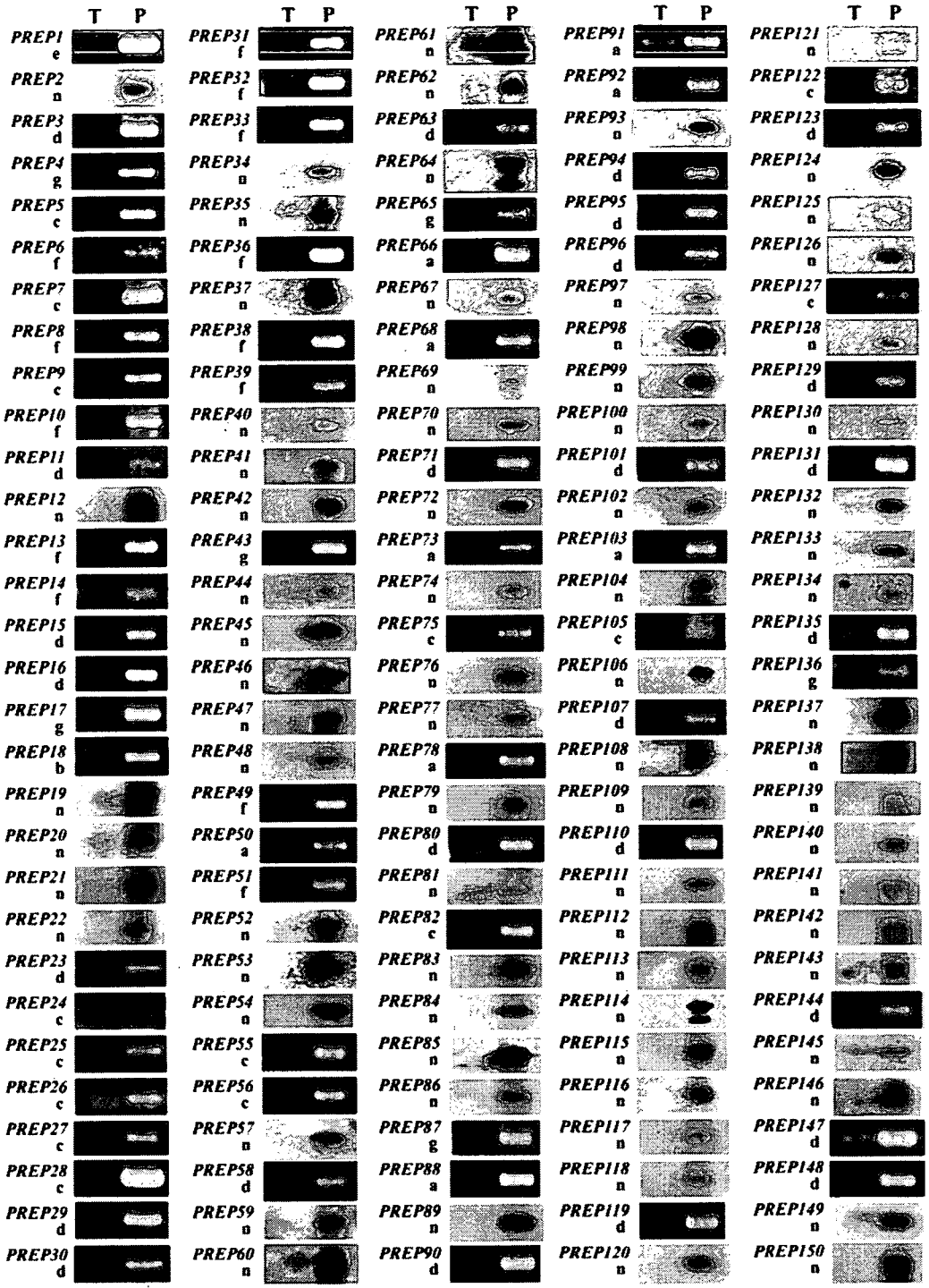

Figure 1. Identification of *PREP* genes. Individual *PREP* cDNA clones were subjected to northern blot or RT–PCR analysis to compare their gene expression levels in the PBMCs of healthy volunteers (right lanes, denoted as P) and human fibroblast TIG-1 cells (left lanes, denoted as T). The names of the *PREP* genes are shown in Table 1. The RT–PCR data for *GAPDH* and the northern blot data for β-actin are also shown as loading controls. The annealing temperature and amplification cycles used in the RT–PCRs are denoted to the left of each image by a–h: a, 50°C and 35 cycles, b, 50°C and 30 cycles, c, 55°C and 35 cycles, d, 55°C and 40 cycles, e, 55°C and 45 cycles, f, 55°C and 30 cycles, and g, 50°C and 40 cycles, respectively. The northern blots are denoted as n.

human fibroblast TIG-1 cells, which are control cells that express non-PBMC transcripts. These mRNAs were biotinylated with photobiotin[7] and used to subtract the PBMC cDNA library as described previously[4] to remove the housekeeping and non-PBMC-specific genes. Briefly, after converting the PBMC cDNA library to a single-stranded form by transfection with f1 helper phage, we hybridized it with the

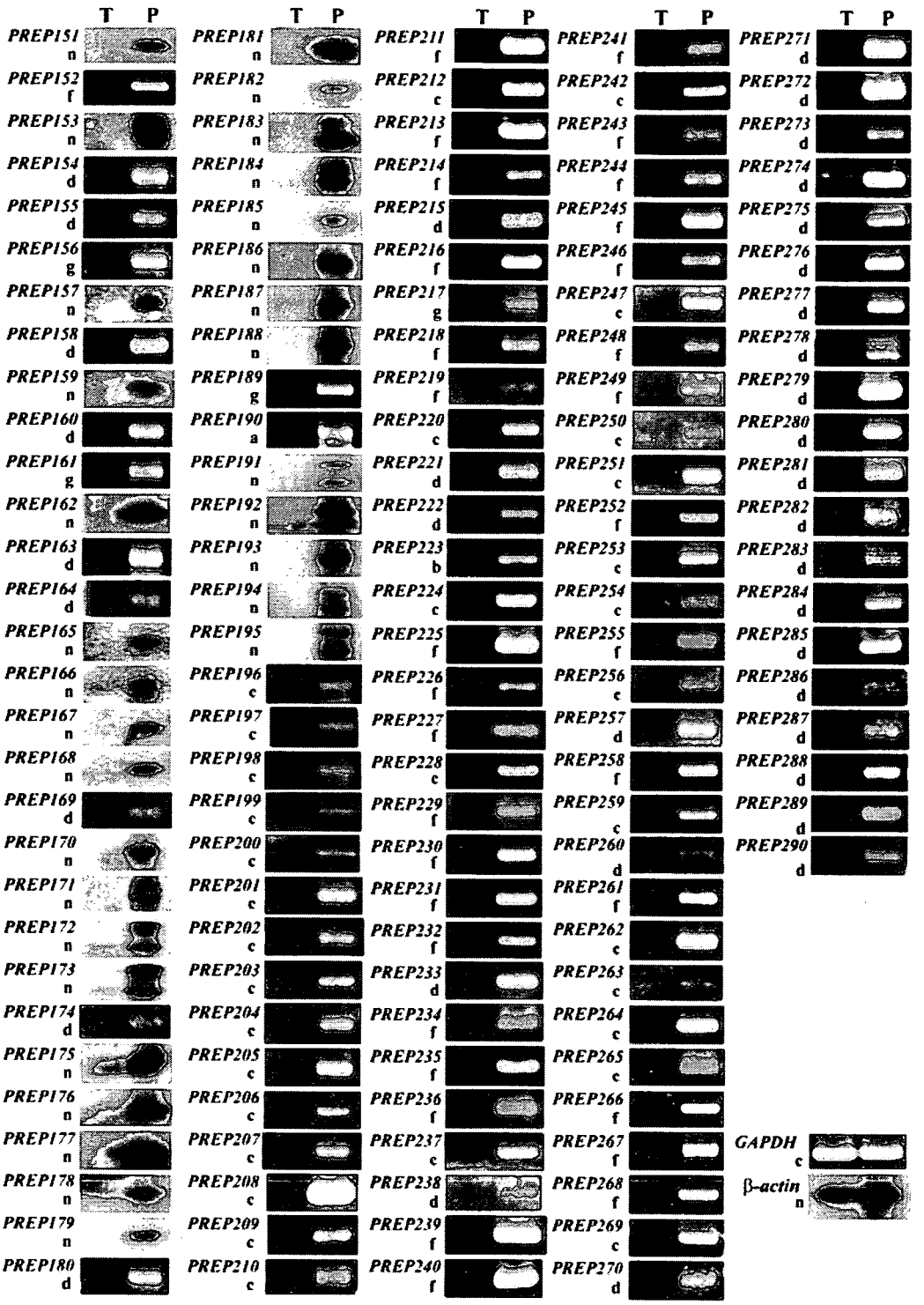

Figure 1. Continued

biotinylated TIG-1 mRNAs and subtracted it by biotin–avidin interactions. The unhybridized clones were converted to the double-stranded form, which was then used to transform competent *E. coli* cells, thereby generating a subtracted cDNA library.

To analyze this subtracted cDNA library, we prepared plasmid DNA from several hundred randomly selected and numbered cDNA clones. An aliquot of each plasmid DNA was then digested with *Eco*RI and *Not*I and their cDNA inserts were purified on 1% agarose gels and fluorescently labeled. These probes were then used in northern analysis to identify those genes whose transcript levels were much higher in PBMCs than in TIG-1 cells, namely, those genes that

showed almost a plus/minus type difference. These genes were named *PREP* after predominantly expressed in PBMC. As shown in Fig. 1, each northern sheet only included two lanes, one each for the RNAs extracted from PBMCs and TIG-1. The DNA sequences of these candidate *PREP* genes were determined from the 5′ end of the cDNA inserts by the dideoxy-chain termination reaction and were used to search the EST database by employing the BLAST algorithm (http://www.ncbi.nlm.nih.gov/BLAST/). For those candidate *PREP* genes whose northern blot signals were weak or undetectable, we examined whether these candidate genes were indeed up-regulated by RT–PCR using oligonucleotide primers based on the DNA sequences of these genes (Supplementary Table S2) (Fig. 1). These procedures were repeated until almost all subtracted cDNAs were tested, as described previously.[4] The end result was the isolation of 197 *PREP* genes.

To reduce the possibility of missing important PBMC-specific pathogenic genes by the stepwise subtraction method, we also performed in parallel a genome-wide cDNA microarray analysis by using Agilent's Hu44K array with the same pooled RNA samples obtained from the PBMCs and TIG-1. The 399 genes that showed the greatest up-regulation in PBMCs compared with TIG-1 were then tested by RT–PCR. This resulted in the identification of 126 *PREP* genes, 33 of which were the same as those obtained by the stepwise subtraction analysis. The candidate *PREP* genes were tested by northern and/or RT–PCR analyses to confirm their PBMC-specifc expression (Fig. 1). We did not test those genes that showed lower up-regulation in PBMCs than the 399 genes because the efficiency of detecting a *PREP* was conspicuously lower in the top 151–400 microarray genes than in the top 1–150 genes. Thus, it appears that while the stepwise subtraction method failed to identify 93 *PREP* genes, the DNA microarray analysis failed to detect 164 *PREP* genes. This disparity is mainly due to the differently sized drivers or probes used for hybridization; cDNA subtraction uses kilobase-order biotinylated mRNA as the driver for subtraction, while DNA microarrays are probed by 60-base oligonucleotides. These data together indicate that we identified 290 *PREP* genes (Supplementary Table S3).

3.2. *Characterization of the unknown* PREP *genes*

Of the 290 *PREP* genes that we identified, *PREP1–PREP50* are uncharacterized genes. Homology and motif search of the gene products (Prep1–Prep50 proteins) using the Motif Scan algorithm (http://myhits.isb-sib.ch/cgi-bin/motif_scan) revealed the following notable motifs in *PREP1–PREP11* (Fig. 2),

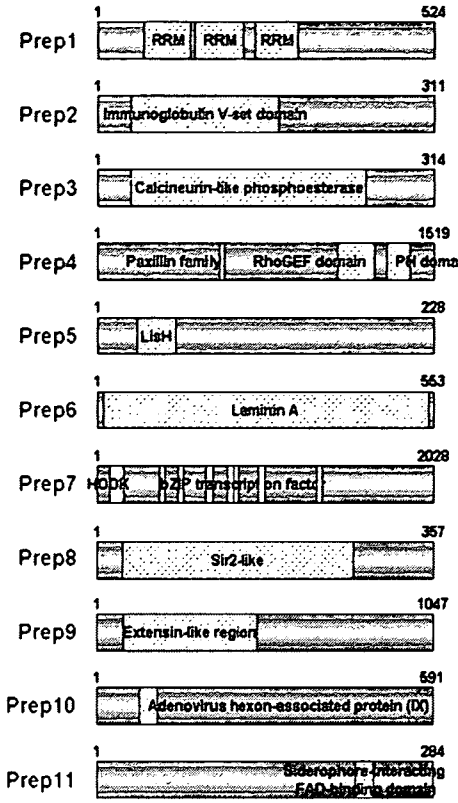

Figure 2. Schematic depiction of the uncharacterized gene products Prep1-Prep11. Numbers indicate the amino acids of the protein. RRM, RNA recognition motif; GEF, Guanine nucleotide exchange factor; PH, pleckstrin homology; LisH, LIS1 (lissencephaly) homology; bZIP, basic region/leucine zipper; Sir2, sirtuin 2; FAD, flavin adenine dinucleotide.

which may suggest their putative physiological functions. The other uncharacterized *PREP* genes did not have any notable motifs.

PREP1 encodes an RNA-binding protein because it harbors three RNA recognition motifs.[8] *PREP2* encodes a protein that harbors a V-set Ig-like domain that is responsible for binding to sialic acid.[9] A specialized subgroup of the Ig superfamily, called sialic acid-binding immunoglobulin-like lectins (Siglecs), can recognize sialylated glycoconjugates and play a role in cell–cell recognition and intracellular signaling. At least 11 related genes have been identified in the human genome, all of which encode type 1 membrane proteins that carry an N-terminal sialic acid-binding V-set Ig domain and varying numbers of C2-set Ig domains.[9] Thus, Prep2 may be a Siglec-type protein. Prep3 protein belongs to the large calcineurin-like phosphoesterase superfamily. Members of this superfamily include the polymerase-associated B-subunits and all carry an active site harboring two divalent metal ions for catalysis.[10] This suggests that Prep3 protein may participate in cell growth by regulating DNA replication. *PREP4*

encodes a novel member of the paxillin family proteins that bear the RhoGEF and PH domains.[11] Paxillin is a multi-domain adaptor that recruits associated proteins to focal adhesions, where it plays a pivotal role in transducing cell signaling, thereby eliciting changes in cell migration and gene expression.[12] Given that the RhoGEF and PH domains both are also found in these cell signaling molecules, Prep4 protein appears to function in the signal transduction of growth signals. *PREP5* encodes a protein with a LisH (LIS1 homology) motif, which is found in many signaling proteins of the WD-40 family and is believed to help regulate microtubule dynamics by mediating dimerization or binding to cytoplasmic dynein heavy chain.[13] Prep6 protein is homologous to laminin A, which is one of the 15 laminin isoforms that are the major component of basement membranes.[14] *PREP7* encodes a basic-leucine zipper (bZip) transcription factor[15] with a DNA-binding motif called AT-hook.[16] *PREP8* encodes a protein that is weakly homologous to Sir2, an NAD-dependent deacetylase that links metabolism with longevity in yeast, flies, and worms.[17] Prep9 protein harbors a region that is weakly homologous to extensin, a hydroxyproline-rich cell wall structural glycoprotein of higher plants.[18] The N-terminal region of Prep10 protein bears a domain that has homology to the adenovirus hexon-associated protein IX.[19] Prep11 protein carries in its C-terminus a domain with homology to the flavin adenine dinucleotide (FAD)-binding domain of siderophore-interacting protein which may be involved in iron chelation and iron utilization.[20]

3.3. *Expression pattern of PREP1–PREP11 and proto-oncogene PREP genes in PBMCs*

To determine whether the uncharacterized *PREP1–PREP11* genes are expressed in particular human blood cells, we performed RT–PCR on multiple tissue cDNA (MTC) panels from Clontech (Palo Alto, CA). As shown in Fig. 3, *PREP3*, *PREP4*, and *PREP6* mRNAs were only detected in resting CD14+ cells (monocytes; M), whereas *PREP1* mRNAs were predominantly found in monocytes but were also faintly expressed in resting CD19+ cells (B cells). In addition, *PREP11* showed a strong signal in monocytes and B cells and a weak signal in T-suppressor/cytotoxic cells and activated CD4+ T cells. *PREP2* was strongly detected in monocytes, T-helper/inducer, and B cells, and weakly in T-suppressor/cytotoxic and activated CD4+ cells. *PREP7* was strongly expressed in all mononuclear cells (B cells, T cells, and monocytes), weakly expressed in activated CD8+ T cells, and faintly expressed in activated CD4+, CD19+, and mononuclear cells. *PREP10* was detected strongly in

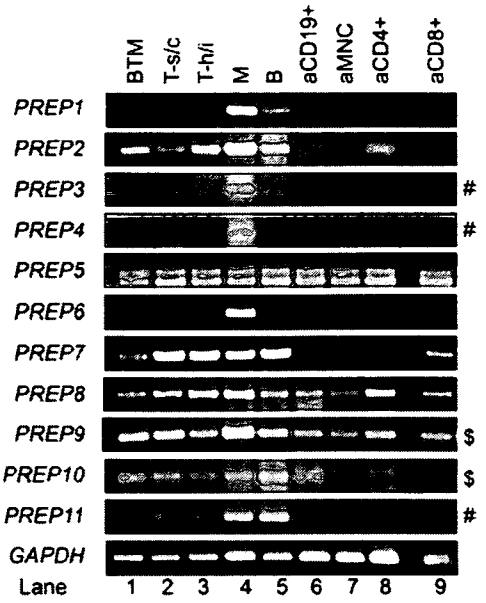

Figure 3. Determination by RT–PCR of the human blood cells that express *PREP1–PREP11*. RT–PCR was performed using a multiple tissue cDNA panel for human blood fractions (MTC, Clontech). *GAPDH* was also amplified as a loading control. PCR amplifications involved 40 cycles at 55°C except as indicated to the right of the panels: 35 cycles at 55°C (#) or 35 cycles at 58°C ($). Lane 1, mononuclear cells (B cells, T cells, and monocytes). Lane 2, resting CD8+ cells (T-suppressor/cytotoxic cells). Lane 3, resting CD4+ cells (T-helper/inducer). Lane 4, resting CD14+ cells (monocytes). Lane 5, resting CD19+ cells (B cells). Lane 6, activated CD19+ cells. Lane 7, activated mononuclear cells (aMNC). Lane 8, activated CD4+ cells. Lane 9, activated CD8+ cells.

all resting mononuclear cells, but only faintly in the other cell types examined. The other *PREP* genes were ubiquitously expressed at almost equal levels in all cell types examined and indeed could serve as a loading control like GAPDH.

Unexpectedly, we found six proto-oncogenes were *PREP* genes, namely, c-*ets*, c-*src*, c-*yes*, c-*fgr*, c-*fos*, and c-*vav*. We initially asked whether the augmented expression of these proto-oncogenes is due to infection-induced T-cell or macrophage stimulation in one of the PBMC donors. To test this, we examined the expression of these proto-oncogenes by RT–PCR on the MTC panel described above, since the sample RNAs used to generate the panel is not the same as our RNAs (Fig. 4). To our surprise, we found all cell types examined strongly expressed c-*ets*, c-*src*, and c-*yes*. All mononuclear cells (B cells, T cells, and monocytes) and activated CD4+ and CD19+ cells, but not activated CD8+ and mononuclear cells, also expressed c-*vav*. In contrast, c-*fgr* was only detected in T-suppressor/cytotoxic cells, while c-*fos* was only detected in resting T-suppressor/cytotoxic cells, B cells, and mononuclear cells. Thus, the expression of these proto-oncogenes is a commonly observed phenomenon.

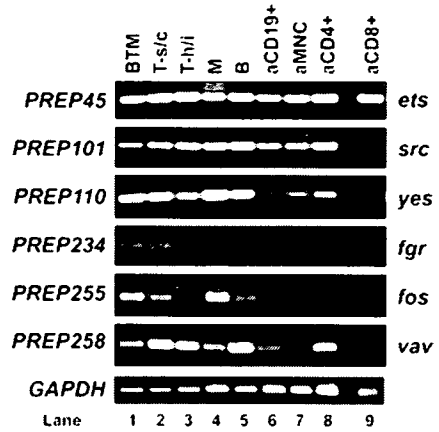

Figure 4. Expression profiles of the indicated proto-oncogenes in human blood fractions. RT–PCR was performed using the multiple tissue cDNA panel (MTC, Clontech). *GAPDH* was also amplified as a loading control. PCR amplifications involved 35 cycles at 55°C for all samples. Lane 1, mononuclear cells (B, T cells and monocytes). Lane 2, resting CD8+ cells (T-suppressor/cytotoxic cells). Lane 3, resting CD4+ cells (T-helper/inducer). Lane 4, resting CD14+ cells (monocytes). Lane 5, resting CD19+ cells (B cells). Lane 6, activated CD19+ cells. Lane 7, activated mononuclear cells (aMNC). Lane 8, activated CD4+ cells. Lane 9, activated CD8+ cells.

3.4. *Focused PREP analysis of CSS PBMCs*

We next examined whether the *PREP* genes can serve in a focused array that can be used to diagnostically. For this purpose, we used the array to determine if CSS patients can be characterized by a particular PREP mRNA expression pattern. CSS is a rare autoimmune disease (ca. 2.4 per million), namely, a small-vessel necrotizing vasculitis that is typically characterized by asthma, lung infiltrates, extravascular necrotizing granulomas, and hypereosinophilia.[21] This disease was chosen because diagnostic gene markers for this disease have not yet been reported. Moreover, it is likely that the symptoms of CSS patients will be reflected in abnormal gene expressions in their PBMCs. Indeed, we found with the aid of expression profiling analysis (GeneSpring) that, compared with normal volunteers, 33 *PREP* genes are consistently up-regulated in the PBMCs of all seven cases of CSS patients tested (Fig. 5A, uppermost panel). Of these, *PREP135*, *PREP77*, *PREP191*, *PREP234*, and *PREP136*, which are highlighted by larger arrows in Fig. 5A, showed the most conspicuous up-regulation in all CSS patients (>2.5-fold change).

PREP135 encodes the coactosin-like protein (CLP), which is a small, evolutionarily conserved F-actin-binding protein that can also bind to 5-lipoxygenase (5LO) and regulate its activity.[22] *PREP77* encodes prosaposin, the precursor of the sphingolipid activator proteins (saposin A, B, C, and D) that are required for the enzymatic hydrolysis of sphingolipids by specific lysosomal hydrolases.[23] *PREP191*, which encodes a lysosomal aspartyl peptidase cathepsin D (CTSD), is known to be involved in prosaposin

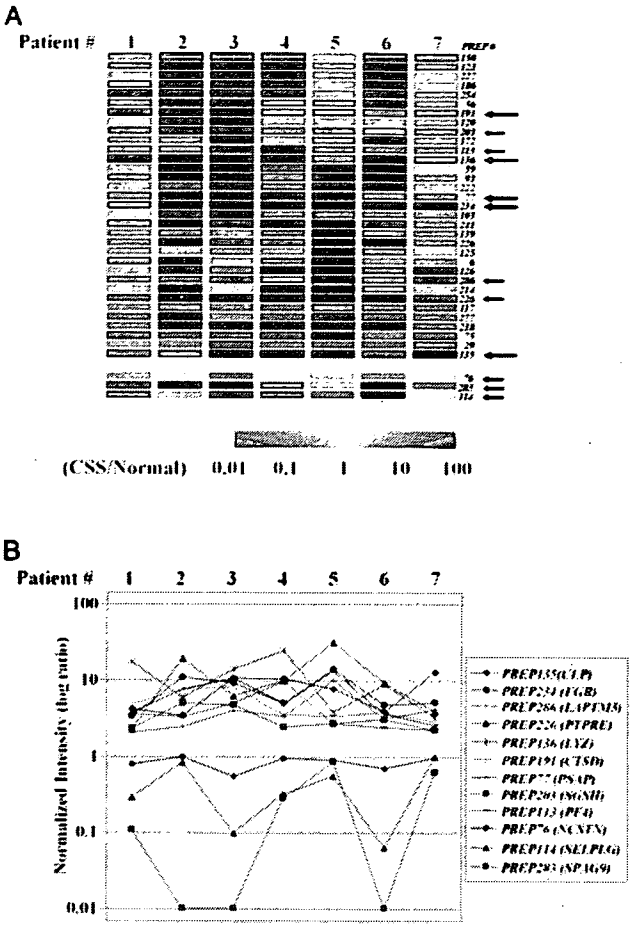

Figure 5. Expression profiles of *PREP* genes in CSS patient PBMCs. Agilent's whole human genome DNA microarray was employed for this analysis. (**A**) Presentation of mosaic tiles for the 33 and 3 *PREP* genes whose expressions are up-regulated (>1.2-fold change) or down-regulated (<1.0-fold change) in all seven CSS patients as compared with healthy volunteers. The gene names are indicated on the right of the panels. The *PREP* genes were selected by a filter and their expressions in all seven cases of CSS patients were grouped together by using GeneSpring software 7.3 (Agilent Technologies, Inc.). In other words, their raw expression values were normalized according to the manufacturer's instructions by conducting a ratio calculation of the two channels. This was followed by a per-gene normalization to ensure all ratios for each gene were normalized to 1. The nine conspicuously up-regulated *PREP* genes (>2.0-fold change) are denoted by arrows; the five large arrows signify more enhanced up-regulation (>2.5-fold change). Tile colors indicate the mean relative transcript level; green corresponds to a log10 ratio of 0.01 (down-regulation), red corresponds to a log10 ratio of 100 (up-regulation), and yellow indicates unchanged (bottom-most panel) when CSS and normal PBMCs are compared (bottom-most panel). (**B**) Graphical presentation of the nine CSS-up-regulated and three CSS-down-regulated *PREP* genes (denoted by arrows in Fig. 5A). Mean values were plotted for the genes that showed a significant ($P < 0.05$) difference in expression. The ordinate scale indicates relative log ratio values.

proteolysis.[24] Thus, the enhanced expression of *PREP77* and *PREP191* suggests sphingolipid levels are increased in CSS. This is consistent with the pivotal role sphingolipids are known to play as proinflammatory factors.[25] Thus, sphingolipids and related enzymes may not only be diagnostic marker for CSS, they may also be novel therapeutic targets in CSS (see Discussion).

PREP234 encodes Gardner–Rasheed feline sarcoma viral (*v*-fgr) oncogene homolog (*c*-fgr: FGR), which is known to play an important role in lipopolysaccharide (LPS)-induced macrophage activation.[26] Indeed, Fgr-deficient mice fail to develop lung eosinophilia in response to repeated challenge with aerosolized ovalbumin (OVA)[27]. Src-family tyrosine kinases are required to support the accumulation of polymorphonuclear leukocytes (PMN) along with adherent platelets at the site of vascular injury.[28] *PREP136* encodes lysozyme, which is one of the genes responsible for autosomal dominant hereditary amyloidosis.[29] Indeed, there are several case reports of amyloidosis associated with CSS that occurs together with a destructive inflammatory or granulomatous reaction to amyloid.[30] Several case reports have also described granulomatous angiitis in patients with sporadic, amyloid beta peptide (Abeta)-related cerebral amyloid angiopathy and Abeta-related angiitis with development of amyloid-associated inflammation.[31]

There are also four other less conspicuously CSS-up-regulated *PREP* genes (2.0–2.5-fold change). Of these, *PREP226* encodes a receptor (membrane)-type variant of the protein tyrosine phosphatase (PTPepsilonM) family protein that negatively regulates insulin receptor (IR) signaling by dephosphorylating IR, thereby suppressing the phosphorylation of IR downstream enzymes such as Akt, extracellular regulated kinase (ERK), and glycogen synthase kinase 3 (GSK3).[32] Notably, the cytosolic isoform of PTPepsilon (PTPepsilonC) selectively inhibits interleukin-6 (IL-6)- and IL-10-induced Janus kinases (JAK)-signal transducer and activator of transcription 3 (STAT3) signaling in blood cells.[33]

Another of the four less conspicuously up-regulated *PREP* genes, *PREP113*, encodes platelet factor 4 (PF4; CXC chemokine ligand 4), which is a specific marker for megakaryocyte cells and that induces the differentiation of monocytes into macrophages during the inflammatory process.[34] *PREP286* encodes lysosomal-associated multi-spanning membrane protein-5 (LAPTM5). While the function of LAPTM5 is unknown, it may participate in host defense in collaboration with other lysosome-related genes (*PREP77*, *PREP191*, and *PREP136*) in the blood cells of CSS patients. These results suggest that the regulation of cell signaling in blood cells from CSS patients is abnormal. The last of the four less conspicuously up-regulated *PREP* genes is *PREP203*, which encodes the spliceosomal protein thioredoxin-like 4B (TXNL4B). However, its physiological significance in the pathogenesis of CSS remains unclear.

We also identified three *PREP* genes that, compared with normal volunteers, are down-regulated in the PBMCs of all seven CSS patients (Fig. 5A, middle panel). *PREP76* encodes nicastrin;[35] its down-regulation may disturb the phagocytic response of macrophages to inflammatory cytokines since gamma-secretase catalyzes the intramembrane cleavage of its protein substrates and targets phagocytosis-related proteins of macrophages.[36] *PREP114* encodes selectin P ligand (SELPLG), which stimulates T lymphocytes, and plays a critical role in the tethering of these cells to activated platelets or endothelia expressing P-selectin.[37] *PREP283* encodes sperm-associated antigen 9 (SPAG9), which has also been identified as a serum target of the autoantibody produced in systemic sclerosis (SSc).[38] Thus, the reduced expression of these three genes could also serve as diagnostic markers of CSS. Unfortunately, we could not correlate the expression levels of these genes to the profiles of tested CSS patients (Supplementary Table S1).

3.5. *Expression pattern of CSS-up-regulated PREP genes in PBMCs*

To examine whether these 12 CSS-up- or -down-regulated *PREP* genes are expressed in particular human blood cells, we performed RT–PCR on MTC panels (Fig. 6). *PREP76*, *PREP135*, and *PREP203* were expressed by nearly all cells, and were the only genes that were expressed by activated CD19+ and activated CD8+ cells. Most of the 12 *PREP* genes were expressed by resting CD14+ cells (monocyte; M) and T-helper/inducer (T-h/i) cells, albeit with different expression levels. All genes except *PREP283* were expressed by T-suppressor/cytotoxic (T-s/c) cells. *PREP76*, *PREP113*, *PREP114*, *PREP135*, and *PREP203* were expressed at varying expression levels by activated mononuclear cells (aMNC). All genes except *PREP114*, *PREP135*, and *PREP283* were expressed by B cells, albeit comparatively weakly. Thus, many of the CSS-up-regulated or -down-regulated *PREP* genes are expressed by T cells or monocytes. Unfortunately, we could not perform the same analysis on CSS patients because of the low numbers of PBMCs available.

4. Discussion

4.1. *Isolation of genes that are predominantly expressed in human PBMCs*

Here we show for the first time (to our knowledge) that RNA diagnostics can be performed by using a

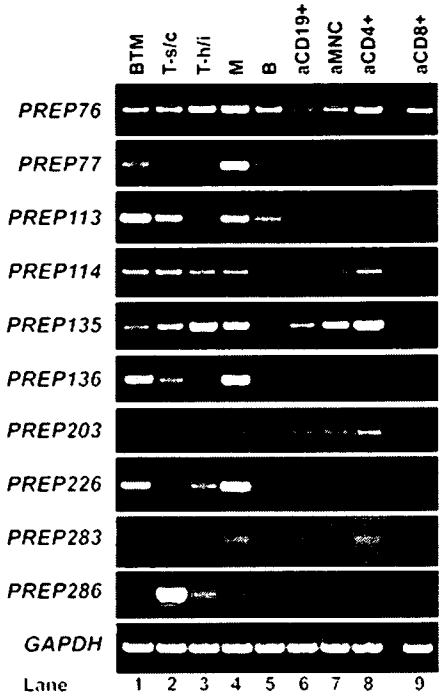

Figure 6. Expression of CSS-up-regulated or -down-regulated *PREP* genes by various human blood cells. RT–PCR was performed with the MTC. The *GAPDH* expression profile served as a loading control. All PCR amplifications involved 35 cycles at 55°C. We could not detect an amplified band for *PREP119* even though we tested three different primer sets (Supplementary Table S1). Lane 1, mononuclear cells (B, T cells and monocytes). Lane 2, resting CD8+ cells (T-suppressor/cytotoxic cells). Lane 3, resting CD4+ cells (T-helper/inducer). Lane 4, resting CD14+ cells (monocytes). Lane 5, resting CD19+ cells (B cells). Lane 6, activated CD19+ cells. Lane 7, activated mononuclear cells (aMNC). Lane 8, activated CD4+ cells. Lane 9, activated CD8+ cells.

PBMC-specific focused array. Such RNA diagnostics methods have the advantage over DNA diagnostics in that ethical problems concerning the genetic information of individuals are avoided. To select the PBMC-specific genes for use in RNA diagnostics, we utilized a technique that we developed previously, namely, stepwise subtraction.[4] In this technique, all genes expressed by a particular cell, tissue, or whole organism are used to generate a cDNA library. This library is then systematically subtracted in a stepwise manner by using the biotinylated mRNAs from a control population to isolate essentially all those genes that are up-regulated relative to the control population expression profile. This technique has proven to be useful for isolating the protein-coding genes that are specifically expressed during cancer metastasis, meiosis, and spermatogenesis, and in patients with autoimmune diseases.[4,39–41] It has also been used to identify putative non-coding RNAs that cannot be identified by microarray screening.[42] By using this technique along with high-density oligonucleotide microarray analysis, we identified 290 *PREP* genes that are predominantly expressed in human PBMCs as compared with fibroblast (TIG-1) cells (Fig. 1 and Table 1). These genes could be used to generate a PBMC-specific focused array that could be used to characterize the abnormal expression profiles in the PBMCs of patients with a particular disease. The abnormal profiles could then serve as a diagnostic tool for other patients presenting with this disease.

The 290 *PREP* genes we identified include 50 uncharacterized genes, 11 of which possess notable amino acid motifs (Fig. 2). Two of these, *PREP1* and *PREP6*, were almost exclusively expressed in monocytes (Fig. 6). Of the 240 *PREP* genes that have been characterized previously, 11, eight, eight, seven, six, five, five, nine, and 36 are HLA genes, CD antigen genes, ribosomal protein genes, interferon (IFN)-related genes, S100 calcium-binding protein-related genes, interleukin (IL)-related genes, platelet-related genes, signal transduction-related genes, and immunity-related genes, respectively (Supplementary Table S4). We did not identify any other immunity-related genes as *PREP* genes by these techniques, probably because their expression levels are lower than the *PREP* genes.

4.2. *PBMC-specific array analysis with CSS patients*

To explore the usefulness of the PBMC-specific focused array analysis in RNA diagnostics, we tested the PBMCs of seven cases of CSS patients.[21] The precise pathogenetic mechanisms of CSS remain elusive, in part because the rarity of this disease. We found that compared with normal volunteers, 22 *PREP* genes were up-regulated by >1.5-fold in the PBMCs of all seven CSS patients (Fig. 5). Of these, *PREP135*, *PREP77*, *PREP191*, *PREP234*, *PREP136*, *PREP203*, and *PREP113* were the most conspicuously up-regulated in CSS patients. How these genes contribute to the pathogenesis of CSS is suggested by the known functions of their products, as follows. *PREP77* (prosaposin) and *PREP135* (CLP) may indicate the enhanced immune responses that cause vascular inflammation; *PREP203* (TXNL4B) and *PREP234* (*c*-fgr) may reflect the augmented intracellular signaling that occurs after an infection causes inflammation; and the increased expression of the lysosome-related genes *PREP77*, *PREP136*, *PREP191*, and *PREP286* may indicate the mounting of an effective defense against invading microorganisms by the lysosomes in blood cells. Thus, our *PREP* gene-focused analysis of CSS patients has helped to identify genes that may be putative diagnostic and/or therapeutic targets.

There are few molecular tools that can be used to aid the diagnosis of CSS. The main tool that is commonly employed is the detection of antineutrophil cytoplasmic autoantibodies (ANCA), which can be

detected by an immunofluorescent assay (IFA) on ethanol-fixed neutrophils. ANCA are associated with systemic necrotizing vasculitis and glomerulonephritis diseases such as CSS, Wegener's granulomatosis (WG), and microscopic polyarteritis (MPA).[43] Two different ANCA immunostaining patterns are observed, namely, a diffuse cytoplasmic staining pattern (c-ANCA) that recognizes proteinase 3, and a perinuclear/nuclear pattern (p-ANCA) that commonly recognizes myeloperoxidase (MPO), which is a neutrophil granule protein that helps generate oxygen radicals and is associated with the antimicrobial properties of neutrophils. The c-ANCA pattern is most frequently observed in WG patients, whereas the p-ANCA pattern is detected in CSS and MPA patients.[44] Notably, ANCAs against alternative antigens such as cathepsin G, which is a major protease released by activated neutrophils, are also occasionally observed.

Since antibodies against cathepsin D (*PREP191*), PTPRE (*PREP226*), FGR (*PREP234*), PF4 (*PREP113*), CLP (*PREP135*), and prosaposin (*PREP77*) are currently commercially available, it may be worthwhile to use these antibodies in IFAs on ethanol-fixed blood cell samples to determine whether these antibodies have a relationship with the ANCA-staining patterns in CSS and whether they can help confirm the diagnosis in ANCA-negative CSS patients. Unfortunately, these experiments will have to be performed in the future because the CSS blood samples we obtained were used up during RNA preparation. Moreover, as CSS occurs only very rarely (only 2.4 patients per 1 million people in Japan), it will take some time to accumulate enough patients for such a study.

Acknowledgements: We thank the patients and healthy volunteers who participated in this study. We also thank Ms. Akie Tanigawa, Ms. Azumi Fujimori, Ms. Tomoko Motoyama, Ms. Kumiko Ikeue, Ms. Maki Masuda, Ms. Yuki Hamada, and Ms. Maki Fukuda for technical assistance, and Dr. Patrick Hughes for critically reading the manuscript.

Supplementary data: Supplementary data are available online at www.dnaresearch.oxfordjournals.org.

Funding

This work was supported in part by grants-in-aid from Bio-Medical Cluster Project In Saito, Innovation Plaza Osaka of the Japan Science and Technology Agency (JST), Scientific Research on Priority Areas 'Applied Genomics', Scientific Research (S), Exploratory Research, and the Science and Technology Incubation Program in Advanced Regions, from the Ministry of Education, Culture, Sports, Science and Technology of Japan to H.N. This study was also supported in part by grants-in-aid from the Ministry of Health and Welfare of Japan to K.S. and H.H.

References

1. Kozal, M. J., Shah, N., Shen, N., et al. 1996, Extensivepolymorphisms observed in HIV-1 clade B protease gene using high-density oligonucleotide arrays, *Nat. Med.*, **2**, 753–759.
2. Trevino, V., Falciani, F. and Barrera-Saldaña, H. A. 2007, DNA microarrays: a powerful genomic tool for biomedical and clinical research, *Mol. Med.*, **13**, 527–541.
3. Kidgell, C. and Winzeler, E. A. 2005, Elucidating genetic diversity with oligonucleotide arrays, *Chromosome Res.*, **13**, 225–235.
4. Fujii, T., Tamura, K., Masai, K., Tanaka, H., Nishimune, Y. and Nojima, H. 2002, Use of stepwise subtraction to comprehensively isolate mouse genes whose transcription is up-regulated during spermiogenesis, *EMBO Rep.*, **3**, 367–372.
5. Masi, A. T., Hunder, G. G., Lie, J. T., et al. 1990, The American College of Rheumatology 1990 criteria for the classification of Churg-Strauss syndrome (allergic granulomatosis and angiitis), *Arthritis Rheum.*, **33**, 1094–1100.
6. Ishii, T., Onda, H., Tanigawa, A., et al. 2005, Isolation and expression profiling of genes upregulated in the peripheral blood cells of systemic lupus erythematosus patients, *DNA Res.*, **112**, 1–11.
7. Kobori, M., Ikeda, Y., Nara, H., et al. 1998, Large scale isolation of osteoclast-specific genes by an improved method involving the preparation of a subtracted cDNA library, *Genes Cells*, **3**, 459–475.
8. Maris, C., Dominguez, C. and Allain, F. H. 2005, The RNA recognition motif, a plastic RNA-binding platform to regulate post-transcriptional gene expression, *FEBS J.*, **272**, 2118–2131.
9. Angata, T., Hingorani, R., Varki, N. M. and Varki, A. 2001, Cloning and characterization of a novel mouse Siglec, mSiglec-F: differential evolution of the mouse and human (CD33) Siglec-3-related gene clusters, *J. Biol. Chem.*, **276**, 45128–45136.
10. Aravind, L. and Koonin, E. V. 1998, Phosphoesterase domains associated with DNA polymerases of diverse origins, *Nucleic Acids Res.*, **26**, 3746–3752.
11. Rathore, V. B., Okada, M., Newman, P. J. and Newman, D. K. 2007, Paxillin family members function as Csk binding proteins that regulate Lyn activity in human and murine platelets, *Biochem. J.*, **403**, 275–281.
12. Brown, M. C. and Turner, C. E. 2004, Paxillin: adapting to change, *Physiol Rev.*, **84**, 1315–1339.
13. Emes, R. D. and Ponting, C. P. 2001, A new sequence motif linking lissencephaly, Treacher Collins and oral-facial-digital type 1 syndromes, microtubule dynamics and cell migration, *Hum. Mol. Genet.*, **10**, 2813–2820.
14. Nguyen, N. M. and Senior, R. M. 2006, Laminin isoforms and lung development: all isoforms are not equal, *Dev. Biol.*, **294**, 271–279.

15. Vinson, C., Acharya, A. and Taparowsky, E. J. 2006, Deciphering B-ZIP transcription factor interactions in vitro and in vivo, *Biochim. Biophys. Acta.*, **1759**, 4–12.
16. Singh, M., D'Silva, L. and Holak, T. A. 2006, DNA-binding properties of the recombinant high-mobility-group-like AT-hook-containing region from human BRG1 protein, *Biol. Chem.*, **387**, 1469–1478.
17. Haigis, M. C. and Guarente, L. P. 2006, Mammalian sirtuins—emerging roles in physiology, aging, and calorie restriction, *Genes Dev.*, **20**, 2913–2921.
18. Diet, A., Link, B., Seifert, G. J., et al. 2006, The Arabidopsis root hair cell wall formation mutant lrx1 is suppressed by mutations in the RHM1 gene encoding a UDP-L-rhamnose synthase, *Plant Cell*, **18**, 1630–1641.
19. Vellinga, J., van-den-Wollenberg, D. J., van-der-Heijdt, S., Rabelink, M. J. and Hoeben, R. C. 2005, The coiled-coil domain of the adenovirus type 5 protein IX is dispensable for capsid incorporation and thermostability, *J. Virol.*, **79**, 3206–3210.
20. Butterton, J. R. and Calderwood, S. B. 1994, Identification, cloning, and sequencing of a gene required for ferric vibriobactin utilization by *Vibrio cholerae*, *J. Bacteriol.*, **176**, 5631–5638.
21. Pagnoux, C., Guilpain, P. and Guillevin, L. 2007, Churg-Strauss syndrome, *Curr Opin. Rheumatol.*, **19**, 25–32.
22. Rakonjac, M., Fischer, L., Provost, P., et al. 2006, Coactosin-like protein supports 5-lipoxygenase enzyme activity and up-regulates leukotriene A4 production, *Proc. Natl. Acad. Sci. USA*, **103**, 13150–13155.
23. Haidar, B., Kiss, R. S., Sarov-Blat, L., et al. 2006, Cathepsin D, a lysosomal protease, regulates ABCA1-mediated lipid efflux, *J. Biol. Chem.* **281**, 39971–39981.
24. Hiraiwa, M., Martin, B. M., Kishimoto, Y., Conner, G. E., Tsuji, S. and O'Brien, J. S. 1997, Lysosomal proteolysis of prosaposin, the precursor of saposins (sphingolipid activator proteins): its mechanism and inhibition by ganglioside, *Arch. Biochem. Biophys.*, **341**, 17–24.
25. Zheng, W., Kollmeyer, J., Symolon, H., et al. 2006, Ceramides and other bioactive sphingolipid backbones in health and disease: lipidomic analysis, metabolism and roles in membrane structure, dynamics, signaling and autophagy, *Biochim. Biophys. Acta.*, **1758**, 1864–1884.
26. Leu, T. H., Charoenfuprasert, S., Yen, C. K., Fan, C. W. and Maa, M. C. 2006, Lipopolysaccharide-induced c-Src expression plays a role in nitric oxide and TNFalpha secretion in macrophages, *Mol. Immunol.*, **43**, 308–316.
27. Vicentini, L., Mazzi, P., Caveggion, E., et al. 2002, Fgr deficiency results in defective eosinophil recruitment to the lung during allergic airway inflammation, *J. Immunol.*, **168**, 6446–6454.
28. Evangelista, V., Pamuklar, Z., Piccoli, A., et al. 2007, Src family kinases mediate neutrophil adhesion to adherent platelets, *Blood*, **109**, 2461–2469.
29. Granel, B., Valleix, S., Serratrice, J., et al. 2007, Lysozyme amyloidosis: report of 4 cases and a review of the literature, *Medicine (Baltimore)*, **85**, 66–73.
30. Meisler, D. M., Stock, E. L., Wertz, R. D., Khadem, M., Chaudhuri, B. and O'Grady, R. B. 1981, Conjunctival inflammation and amyloidosis in allergic granulomatosis and angiitis (Churg-Strauss syndrome), *Am. J. Ophthalmol.*, **91**, 216–219.
31. Scolding, N. J., Joseph, F., Kirby, P. A., et al. 2005, Abeta-related angiitis: primary angiitis of the central nervous system associated with cerebral amyloid angiopathy, *Brain*, **128**, 500–515.
32. Nakagawa, Y., Aoki, N., Aoyama, K., et al. 2005, Receptor-type protein tyrosine phosphatase epsilon (PTPepsilonM) is a negative regulator of insulin signaling in primary hepatocytes and liver, *Zoolog. Sci.*, **22**, 169–175.
33. Tanuma, N., Shima, H., Nakamura, K. and Kikuchi, K. 2001, Protein tyrosine phosphatase epsilonC selectively inhibits interleukin-6- and interleukin- 10-induced JAK-STAT signaling, *Blood*, **98**, 3030–3034.
34. Scheuerer, B., Ernst, M., Durrbaum-Landmann, I., et al. 2000, The CXC-chemokine platelet factor 4 promotes monocyte survival and induces monocyte differentiation into macrophages, *Blood*, **95**, 1158–1166.
35. Shah, S., Lee, S. F., Tabuchi, K., et al. 2005, Nicastrin functions as a gamma-secretase-substrate receptor, *Cell*, **122**, 435–447.
36. Jutras, I., Laplante, A., Boulais, J., Brunet, S., Thinakaran, G. and Desjardins, M. 2005, Gamma-secretase is a functional component of phagosomes, *J. Biol. Chem.*, **280**, 36310–36317.
37. Hirata, T., Furukawa, Y., Yang, B. G., et al. 2004, Human P-selectin glycoprotein ligand-1 (PSGL-1) interacts with the skin-associated chemokine CCL27 via sulfated tyrosines at the PSGL-1 amino terminus, *J. Biol. Chem.*, **279**, 51775–51782.
38. Yasuoka, H. and Kuwana, M. 2007, Autoantibody response against a novel testicular antigen protein highly expressed in testis (PHET) in SSc patients, *Autoimmun. Rev.*, **6**, 228–231.
39. Ito, A., Katoh, F., Kataoka, T. R., et al. 2000, A role for heterologous gap junctions between melanoma and endothelial cells in metastasis, *J. Clin. Invest.*, **105**, 1189–1197.
40. Watanabe, T., Miyashita, K., Saito, T. T., et al. 2001, Comprehensive isolation of meiosis-specific genes identifies novel proteins and unusual non-coding transcripts in *Schizosaccharomyces pombe*, *Nucleic Acids Res.*, **29**, 2327–2337.
41. Nakamura, N., Shimaoka, Y., Tougan, T., et al. 2006, Isolation and expression profiling of genes upregulated in bone marrow-derived mononuclear cells of rheumatoid arthritis patients, *DNA Res.*, **13**, 169–183.
42. Watanabe, T., Miyashita, K., Saito, T. T., Nabeshima, K. and Nojima, H. 2002, Abundant poly(A)-bearing RNAs that lack open reading frames in Schizosaccharomyces pombe, *DNA Res.*, **9**, 209–215.
43. Radice, A. and Sinico, R. A. 2005, Antineutrophil cytoplasmic antibodies (ANCA), *Autoimmunity*, **38**, 93–103.
44. Kallenberg, C. G., Heeringa, P. and Stegeman, C. A. 2006, Mechanisms of Disease: pathogenesis and treatment of ANCA-associated vasculitides, *Nat. Clin. Pract. Rheumatol.*, **2**, 661–670.

EUKARYOTIC CELL, June 2007, p. 971–983 Vol. 6, No. 6
1535-9778/07/$08.00+0 doi:10.1128/EC.00016-07

Mcp4, a Meiotic Coiled-Coil Protein, Plays a Role in F-Actin Positioning during *Schizosaccharomyces pombe* Meiosis[▽]

Ayami Ohtaka, Daisuke Okuzaki, Takamune T. Saito,† and Hiroshi Nojima*

Department of Molecular Genetics, Research Institute for Microbial Diseases, Osaka University, 3-1 Yamadaoka, Suita City, Osaka 565-0871, Japan

Received 17 January 2007/Accepted 26 March 2007

Some meiosis-specific proteins of *Schizosaccharomyces pombe* harbor coiled-coil motifs and play essential roles in meiotic progression. Here we describe Mcp4, a novel meiosis-specific protein whose expression is abruptly induced at the horsetail phase and which remains expressed until sporulation is finished. Fluorescence microscopic analysis revealed that Mcp4 alters its subcellular localization during meiosis in a manner that partially resembles the movement of F-actin during meiosis. Mcp4 and F-actin never colocalize; rather, they are located in a side-by-side manner. When forespore membrane formation begins at metaphase II, the Mcp4 signals assemble at the lagging face of the dividing nuclei. At this stage, they are sandwiched between F-actin and the nucleus. Mcp4, in turn, appears to sandwich F-actin with Meu14. In *mcp4*Δ cells at anaphase II, the F-actin, which is normally dumbbell-shaped, adopts an abnormal balloon shape. Spores of *mcp4*Δ cells were sensitive to NaCl, although their shape and viability were normal. Taken together, we conclude that Mcp4 plays a role in the accurate positioning of F-actin during *S. pombe* meiosis.

The generation of heritable haploid gametes from diploid parental cells requires meiosis. When fission yeast (*Schizosaccharomyces pombe*) cells are starved by nitrogen deprivation, two haploid cells with opposite mating types conjugate, after which their nuclei fuse together and then undergo meiosis. This begins with a single round of DNA replication, after which the nucleus begins to oscillate between the cell poles and quickly acquires an elongated shape called the horsetail. At this stage, homologous chromosome pairing and genetic recombination occur. The cells then undergo two rounds of continuous cell division, called meiosis I and meiosis II, after which they start to form the double-layer forespore membrane (FSM) (29). Subsequently, during sporulation, the FSM grows into spore walls. Thus, one cell produces one ascus containing four spores. The spores then await appropriate environmental conditions before starting vegetative growth.

The FSM encapsulates the haploid nuclei and serves as the scaffold for spore wall materials. The formation of FSMs starts on the cytoplasmic side of the spindle pole body (SPB) and goes on to wrap each divided nucleus along with cellular organelles by fusing with membranous vesicles derived from the endoplasmic reticulum (ER) via the Golgi apparatus (15). The spore walls are formed by sorting the cell wall components to the luminal space between the outer and inner layers of the FSMs. After the spore wall is successfully organized, mature spores are released from the ascus by autolysis of the ascal cell wall. The movement of the nascent FSM has been determined by studying the behavior of the green fluorescent protein (GFP)-tagged FSM protein Psy1 under a microscope (15). GFP-Psy1 localizes to the plasma membrane before meiosis I and then suddenly disappears before reappearing at the cytoplasmic face of the SPB at metaphase II. Subsequently, it surrounds each of the nuclei. By the time the FSM is closed, GFP-Psy1 surrounds each haploid nucleus. *S. pombe* spores, which resume vegetative growth when appropriate nutrients are supplied, are more resistant to organic solvents and freezing than are mitotic cells (28). This process, called germination, might correspond to the transition from the quiescent G_0 phase to active proliferation in higher eukaryotes. Germinated spores grow out initially by cell expansion, followed by unidirectional cell extension. Cortical actin patches are randomly distributed in the early stage of outgrowth and then localize to one side of spores before the formation of projections (4).

F-actin plays an essential role in the life of *S. pombe* (19), and its subcellular movement during meiosis has been analyzed in detail (7, 20). Briefly, after meiosis is induced by cell fusion and the cells enter the horsetail phase, F-actin appears as randomly scattered dots. These dots remain scattered during meiosis I, but when the cells proceed to prometaphase or metaphase of meiosis II, they accumulate around the two nuclei. Subsequently, during anaphase II, when the two nuclei both divide in two, F-actin is detected at the extending rim of the cup-shaped FSM. This region of the FSM has been designated the "leading edge" of the FSM (18), where Meu14 and F-actin are partly colocalized (7). By early anaphase II, F-actin is also detected on the opposite side of the nucleus, in the vicinity of the SPB. Finally, in the spores of the mature ascus, F-actin again adopts a scattered localization. During sporulation in budding yeast, i.e., *Saccharomyces cerevisiae*, actin is essential for maturation of the spore wall but not for the assembly, shaping, and closure of the prospore membrane, which corresponds approximately to the fission yeast FSM (31).

We previously reported that the meiosis-specific *S. pombe* proteins Meu13 (14) and Meu14 (18) harbor coiled-coil motifs.

* Corresponding author. Mailing address: Department of Molecular Genetics, Research Institute for Microbial Diseases, Osaka University, 3-1 Yamadaoka, Suita City, Osaka 565-0871, Japan. Phone: 81-6-6875-3980. Fax: 81-6-6875-5192. E-mail: snj-0212@biken.osaka-u.ac.jp.

† Present address: Department of Genetics, Harvard Medical School, 77 Avenue Louis Pasteur, New Research Building, Room 334, Boston, MA 20115.

▽ Published ahead of print on 13 April 2007.

TABLE 1. Strains used in this study

Strain	Genotype	Source
CD16-1	*h⁺/h⁻ ade6-M210/ade6-M216 cyh1/⁺ ⁺/lys5-391*	C. Shimoda
CD16-5	*h⁻/h⁻ ade6-M210/ade6-M216 cyh1/⁺ ⁺/lys5-391*	C. Shimoda
TP4-5A	*h⁻ ade6-M210 leu1-32 ura4-D18*	C. Shimoda
TP4-1D	*h⁺ ade6-M216 his2 leu1-32 ura4-D18*	C. Shimoda
AO24	*h⁻ ade6-M210 leu1-32 ura4-D18 mcp4::ura4⁺*	This study
AO28	*h⁺ ade6-M216 his2 leu1-32 ura4-D18 mcp4::ura4⁻*	This study
AO89	*h⁻/h⁻ ade6-M210/ade6-M216 ura4-D18/ura4-D18 leu1-32/leu1-32 pat1-114/pat1-114 mcp3::[mcp3⁺-*9myc-3′UTR-*LEU2]/mcp3::[mcp3⁺-9myc-3′UTR-*LEU2] mcp4::[mcp4-*3ha-3′UTR-*ura4⁺]/mcp4::[mcp4⁺-3ha-3′UTR-*ura4⁺]*	This study
AO64	*h⁹⁰ ade6-M210 leu1-32 ura4-D18 mcp4::[mcp4⁺-*3ha-3′UTR-*ura4⁻]*	This study
AO00	*h⁹⁰ leu1-32* pRGT41-*mcp4⁺*	This study
YN68	*h⁹⁰ leu1::[gfp-psy1⁺-leu1⁻]*	C. Shimoda
AO185	*h⁹⁰ ade6-M210 leu1-32 ura4-D18 mcp4::[mcp4⁺-*3ha-3′UTR-*ura4⁻] meu14::ura4⁺*	This study
AO187	*h⁹⁰ ade6-M210 leu1-32 ura4-D18 mcp4::[mcp4⁺-*3ha-3′UTR-*ura4⁻] meu14::meu14⁺-gfp*	This study
AO192	*h⁹⁰ ade6-M210 leu1-32 ura4-D18* (or ⁻) *mcp4::[mcp4-*3ha-3′UTR-*ura4⁺] crn1⁺-gfp::kanMX6*	This study
AO189	*h⁹⁰ leu1-32 ura4-D18 mcp4::ura4⁻* pRGT41-*mcp4⁺*	This study
AO190	*h⁹⁰ leu1-32 ura4-D18 mcp4::ura4⁻* pRGT41-*mcp4ΔC*	This study
AO125	*h⁹⁰ leu1::gfp-psy1⁻ ura4-D18* (or ⁺) *mcp4::ura4⁺*	This study
AO181	*h⁹⁰ leu1-32* pRGT41-*mcp4ΔC*	This study
FY13596[a]	*h⁹⁰ crn1⁺-gfp*::Kan[r] *ade6-M210 leu1-32*	YGRC/NBRP
AO168	*h⁹⁰ ade6-M210 leu1-32* pREP1-*rer1⁺-cfp ura4-D18* pRGT2-*mcp4ΔC*	This study
AO165	*h⁺ ade6-M216 leu1-32 his2 ura4-D18 lys3 cdc12 mcp4::ura4⁺*	This study
AO162	*h⁻ ade6-M210 ura4-D18 mcp4::ura4⁺*	This study
AO194	*h⁹⁰ ade6-M210 leu1-32 ura4-D18 mcp4::[mcp4⁺-*3ha-3′UTR-*ura4⁻]* pREP81-*gfp-psy1*	This study
AO196	*h⁹⁰ ade6-M210 leu1-32 ura4-D18 mcp4::[mcp4⁺-*3ha-3′UTR-*ura4⁻] spn6-gfp*::Kan[r]	This study
AO200	*h⁹⁰ leu1-32 ura4-D18 mcp4::[mcp4⁻-*3ha-3′UTR-*ura4⁺] cut15-gfp::LEU2*	This study
ST272	*h⁺ ade6-M210 his2 leu1-32 ura4-D18 lys3 cdc12*	Our stock
NP16-6B	*h⁻ ade6-M216 ura4-D18*	Our stock
AO54	*h⁻ ura4-D18 mcp4::ura4⁺*	This study
AO122	*h⁺ his2 leu1-32 ura4-D18 lys3 cdc12 mcp4::ura4⁺*	This study
MS105-1B	*h⁻ ade6-M26 ura4-D18*	Our stock
MS111w1	*h⁺ ade6-469 ura4-D18 leu1-32 his2*	Our stock
TT8-1	*h⁻ ura4⁺*	Our stock
NP32-2A	*h⁺ leu1-32 his2 ura4-D18*	Our stock
AO127	*h⁻ ade6-M26 ura4-D18 mcp4::ura4⁺*	This study
AO128	*h⁺ his2 ade6-469 ura4-D18 mcp4::ura4⁺*	This study
JZ670	*h⁻/h⁻ ade6-M210/ade6-M216 ura4-D18/ura4-D18 leu1-32/leu1-32 pat1-114/pat1-114*	M. Yamamoto
AO115	*h⁻/h⁻ ade6-M210/ade6-M216 ura4-D18/ura4-D18 leu1-32/leu1-32 pat1-114/pat1-114 mcp4::ura4⁺/mcp4::ura4⁺*	This study
AO56	*h⁹⁰ ade6-M210 leu1-32 ura4-D18 mcp4::[mcp4⁺-gfp-*3′UTR-*ura4⁺]*	Our stock

[a] This strain was obtained from the Yeast Genetic Resource Center of Japan, supported by the National BioResource Project (YGRC/NBRP [http://yeast.lab.nig.ac.jp/nig/]).

Meu13 plays a pivotal role in homologous pairing and meiotic recombination at meiosis I as well as in the meiotic recombination checkpoint (27). Meu14 localizes at the leading edge of the FSM and is essential for accurate FSM formation. Another protein known to regulate spore formation in *S. pombe*, namely, Spo15 (6), also contains coiled-coil regions. The coiled-coil motif is important for protein-protein interactions (13). These observations suggested to us that other novel meiosis-specific proteins that play key roles in meiosis by interacting with each other could be identified by screening for coiled-coil proteins whose expression is specifically induced during *S. pombe* meiosis. Indeed, our comprehensive screening yielded a number of novel *m*eiotic *c*oiled-coil *p*rotein (Mcp)-encoding genes (21). We have subsequently shown that one of these, Mcp7, associates with Meu13 and is required for meiotic recombination in *S. pombe* (21). In addition, Mcp6/Hrs1 localizes at the SPB and is needed for establishing the proper astral microtubule positioning that maintains the horsetail movement of the nucleus (22, 30). Mcp5, the homolog of the budding yeast dynein anchor Num1, localizes to the cell cortex and functions as a dynein anchor that facilitates horsetail movement (23, 32). Here we describe the role that Mcp4 plays in *S. pombe* meiosis. Our studies show that it regulates the proper positioning of F-actin during FSM formation.

MATERIALS AND METHODS

Yeast strains, media, and molecular biology. The *S. pombe* strains used in this study are listed in Table 1. The complete media yeast extract-peptone-dextrose (YPD) and yeast extract (YE), synthetic Edinburgh minimal medium 2 (EMM2), and the sporulation media molt extract (ME) and EMM2-nitrogen (EMM2-N) were used. Induction of synchronous meiosis was assessed as described previously (27). We used the high-copy-number plasmid pRGT41 driven by its *nmt41* promoter for overproduction experiments (18).

Gene disruption of *mcp4⁺*. We disrupted the *mcp4⁺* gene by replacing it with the *ura4⁺* cassette according to a previously described method (22). Briefly, we made two pBSK-GD-Mcp4 primers consisting of 100 bp from either end of the *mcp4⁺* gene; each primer was also flanked with 20 bp of the *ura4⁺*-containing pBluescript II KS(+) vector sequence, as follows: forward primer, 5′-TCAAAG CAGGCTTAAAAAAAGATGATATAAAATAATTCTAAAGAATACCGAA GTTAATTAATTTTTAAATCTGCATTCTGGGATTGATTACTCATTATA ATGCAGGAATTCGATATCAAG-3′; and reverse primer, 5′-ATGCTTGAA CAGAGCTTTTAAAAACTATTTCATCCCAAAATATAGGATGAACTTCA AATCGAGAAAATTGGGAAAAAAGTAAATTAATGAAATACAAAATA GGTCGACGGTATCGATAAG-3′. The underlined sequences belong to the pBluescript II KS(+) vector. The primers generated a 2.0-kb PCR product

containing the *ura4*$^+$ cassette. This product was introduced into the haploid strains TP4-5A and TP4-1D, and the Ura$^+$ transformants were screened by PCR analysis to identify the *mcp4*::*ura4*$^+$ strain. All of the mutants that were isolated were backcrossed three times with the wild-type strains.

Construction of Mcp4-3HA-expressing strain. To prepare the Mcp4-3HA construct, we performed PCR and obtained a DNA fragment carrying the open reading frame (ORF) and 3′ downstream region of the *mcp4*$^+$ gene. The following primers were used to obtain the Mcp4 ORF: mcp4 ORF-F (5′-CATAT GGAGCCCTGTGAAGACAAATG-3′) and mcp4 ORF-R (5′-GCGCGGCCG CGGTTCGTTTTCATTAGGCAGAG-3′). The underlined sequences denote the artificially introduced restriction enzyme sites for NdeI and NotI, respectively. The following primers were used to obtain the 3′ downstream region: mcp4 3′UTR-F (5′-GCCCCGGGATTTTGTATTTCATTAATTTAC-3′) and mcp4 3′UTR-R (5′-GCGAGCTCATTCACGACCTTCATGTTCTATTG-3′). The underlined sequences denote the artificially introduced restriction enzyme sites for SmaI and SacI, respectively. The 3′ downstream region was inserted into the 3HA-containing pREP vector via SmaI-SacI, cut out by NotI-EcoRI, and then inserted into the pT7 BlueT vector containing the Mcp4 ORF. The construct was then cut out by EcoRI-SpeI and inserted into the *ura4*$^+$-containing pBluescript II KS(+) vector, which was subsequently digested with PstI and introduced into the haploid strain TP4-1D. The Ura$^+$ transformants were then screened by PCR.

Fluorescence microscopic observation and immunofluorescence. Fluorescence microscopic observations were performed as described previously (22). Cells were cultured in 10 ml EMM2 with supplements until they reached mid-log phase at 28°C. The cells were collected by centrifugation, washed three times with 1 ml EMM2-N, and induced to enter meiosis by incubation in EMM2-N at 28°C for 10 h. For immunofluorescence experiments, meiotic cells were fixed after the procedure, using glutaraldehyde. For glutaraldehyde fixation, 10 ml of cultured cells was incubated in 3% paraformaldehyde and 0.25% glutaraldehyde for 1 h. For indirect immunofluorescence microscopy, microtubules were stained with the anti-α-tubulin antibody TAT1 (a gift from K. Gull, University of Manchester, Manchester, United Kingdom), the SPB was stained with an anti-Sad1 antibody (a gift from O. Niwa, Kazusa DNA Research Institute, Kisarazu, Japan), and Mcp4-3HA was stained with a rat anti-hemagglutinin (anti-HA) antibody (Boehringer Mannheim, Germany). Subsequently, we added an Alexa 488-conjugated goat anti-mouse antibody (Invitrogen) for TAT1, an Alexa 488-conjugated goat anti-rabbit antibody (Invitrogen) for the anti-Sad1 antibody, and an Alexa 594-conjugated goat anti-rat immunoglobulin G (Molecular Probes Inc.) for the anti-HA antibody. The samples were then stained with 0.2 mg/ml Hoechst 33342 in phosphate-buffered saline (PBS; 150 mM NaCl, 40 mM K_2HPO_4, and 10 mM KH_2PO_4) for 1 min and mounted with antifade mounting medium containing *p*-phenylenediamine. Fluorescence images of these cells were observed using a fluorescence microscope (BX51; Olympus) with a charge-coupled device camera (CoolSNAP; Roper Scientific). Immunofluorescence images were acquired using Photoshop 7.0 (Adobe). The Golgi complex/endosome and vacuoles of fission yeast wild-type and mutant cells were labeled with FM4-64 (Molecular Probes Inc.) (see below).

FM4-64 and rhodamine-phalloidin staining. To visualize the fission yeast vacuole, the cells were labeled with the lipophilic dye FM4-64 according to the method described by Kita et al. (9), with some modifications. Briefly, the cells were grown to the exponential phase in EMM or induced to enter meiosis in EMM-N at 28°C, after which the two cell populations were harvested by centrifugation at 4°C and resuspended in ice-cold EMM or EMM-N. FM4-64 was added to a final concentration of 80 μM, and the cells were incubated at room temperature for 15 min. Thereafter, the cells were harvested by centrifugation at 700 × *g* for 3 min at 4°C, washed by resuspension in ice-cold fresh EMM or EMM-N to remove free FM4-64, and incubated at room temperature. The cells were then harvested after 5 min to visualize the Golgi complex/endosomes or after 60 min to visualize the vacuoles, washed with ice-cold PBS, and immediately examined under a fluorescence microscope.

To visualize F-actin, rhodamine-phalloidin staining was performed by using the method of Sawin and Nurse (26), with some modifications. Briefly, growing cultures were added directly to a 1/6 volume of prewarmed 30% electron microscopy (EM)-grade formaldehyde and fixed for 1 h at 28°C. The cells were then washed three times in one culture volume of 0.1 M Na-PIPES, pH 6.8, 1 mM EGTA, and 1 mM $MgCl_2$ (PEM), extracted for 30 s with PEM–1% Triton X-100, and washed three additional times with PEM. Three hundred units of rhodamine-phalloidin (Molecular Probes) was resuspended in 1.5 ml methanol, divided into 15-μl aliquots, evaporated in a Speed-Vac machine, and stored at −20°C. For staining, one aliquot was resuspended in 50 μl PEM, and 7 μl of this was added to no more than 1 μl of fixed, extracted cell pellet. For mounting, 0.5 μl of stained cells was spotted onto a glass slide, followed by 2.5 μl of PEM mounting medium containing 1 mg/ml *p*-phenylenediamine as an antifade agent.

Sensitivity to NaCl. Homothallic haploid cells were grown on yeast extract-peptone-dextrose plates at 33°C, and the cells were mated and sporulated on ME plates at 28°C for 4 days. At the end of the culture, the ascal walls were spontaneously dissolved, and single spores were liberated. The spores were separated on YE plus histidine (YEH) agar plates, with or without 0.1 M or 0.17 M NaCl, by use of a micromanipulator (Singer Instruments, Somerset, United Kingdom). The plates were incubated at 30°C for 5 days, after which NaCl sensitivity was calculated.

RESULTS

***mcp4*$^+$ is a meiosis-specific gene that generates a coiled-coil protein.** *mcp4*$^+$ is one of the seven genes encoding meiosis-specific coiled-coil proteins that we isolated by our screening analysis, as reported previously (21). Mcp4 consists of 355 amino acids and harbors a putative coiled-coil motif close to its C terminus (Fig. 1A). Homology searches using the BLAST algorithm (http://www.ncbi.nlm.nih.gov/BLAST/) failed to identify orthologues in other organisms, which indicates that Mcp4 is specific to *S. pombe*.

We first investigated the meiotic expression pattern of *mcp4*$^+$ by Northern blot analysis, using RNAs obtained from CD16-1 (*h*$^+$/*h*$^+$) and CD16-5 (*h*$^-$/*h*$^-$) cells harvested at various times after commencement of nitrogen starvation. CD16-1 cells undergo meiosis upon nitrogen starvation, unlike CD16-5 cells. This analysis revealed that *mcp4*$^+$ displays meiosis-specific transcription that starts just before the nuclear division in meiosis I (i.e., 6 h after induction) (Fig. 1B). This result confirms a previous report showing that *mcp4*$^+$ transcription is elevated severalfold during the meiosis I nuclear division (11).

To accurately examine the expression of the Mcp4 protein during meiosis, we constructed the *mcp4*$^+$-3ha strain, which expresses the Mcp4 protein tagged with three copies of the HA epitope at its C-terminal end. To obtain synchronized meiotic progression, we replaced the *mcp4*$^+$ gene of the *pat1-114* strain with the *mcp4*$^+$-3ha fusion gene. The *pat1-114 mcp4*$^+$-3ha diploid cells were then induced to enter synchronized meiosis by a temperature shift, and their lysates were subjected to Western blot analysis using the anti-HA antibody as the probe. We first confirmed that the meiotic progression and spore morphology of *pat1-114 mcp4*$^+$-3ha and *pat1-114* diploid cells were similar (data not shown). Western blot analysis showed that the Mcp4-3HA protein migrated at the expected size and was expressed only during meiosis, from 2.5 to 8 h after the temperature shift (Fig. 1C). In other words, the Mcp4-3HA protein was first observed at the horsetail phase and remained detectable until sporulation occurred. This timing of Mcp4 expression is considered to be more accurate than the result obtained by Northern blotting using the CD16-1 strain (Fig. 1B) because synchronized meiosis is accurate when the *pat1-114* strain is used. This means that Mcp4 appears only 30 min after Meu13 becomes detectable. Meu13 is another meiosis-specific coiled-coil protein that regulates the meiotic recombination checkpoint (27) and plays a pivotal role in homologous pairing and meiotic recombination at meiosis I (14).

Mcp4-3HA is detected as cytoplasmic dots during meiosis. To examine the subcellular localization of the Mcp4 protein during meiosis, we utilized the homothallic haploid AO64 strain (*h*^{90} *mcp4*$^+$-3ha), which can be visualized under a fluorescence microscope. Mcp4-3HA expression did not impair meiotic progression

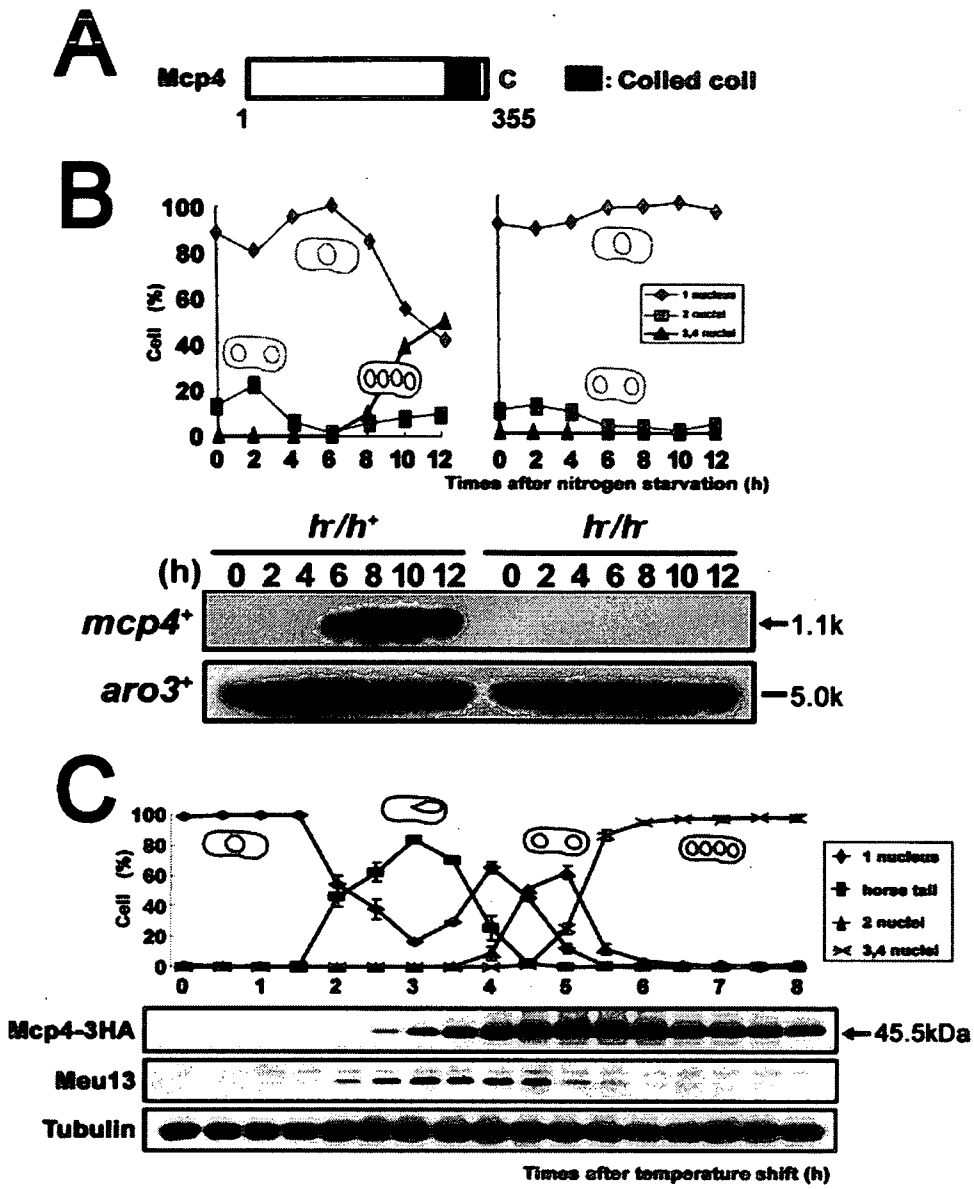

FIG. 1. Mcp4 is a meiosis-specific coiled-coil protein. (A) Schematic depiction of Mcp4 (355 amino acids). The predicted coiled-coil motif was identified by PSORT II (http://psort.nibb.ac.jp/) and is indicated by the black box. (B) Meiotic expression of *mcp4*$^+$. h^+/h^- (CD16-1) and h^-/h^- (CD16-5) diploid cells were subjected to nitrogen starvation, which induces CD16-1 but not CD16-5 cells to enter meiosis. The cells were collected at 2-h intervals, and the total RNAs were blotted and probed with the *mcp4*$^+$ ORF. The RNAs were also probed with the *aro3*$^+$ ORF as a loading control. (C) Meiotic expression of Mcp4-3HA. The h^-/h^- *pat1-114 mcp4*$^+$-3ha strain (AO89) was induced to enter meiosis synchronously by a temperature shift, and the cells were collected at 30-min intervals for protein extraction, blotting, and probing with anti-HA antibody. Meu13 expression was also analyzed by using an anti-Meu13 antibody to help identify the meiotic stage at each time point. The tubulin levels were also examined as a loading control. At each time point in panels B and C, the frequency of cells with one, two, three, or four nuclei was determined by counting at least 200 Hoechst 33342-stained cells under a microscope. The upper panels show the stages of meiosis.

and spore formation (data not shown), which indicates that the tagged Mcp4 protein is fully functional. Cells carrying *mcp4*$^+$-3ha were induced to enter meiosis and were fixed before Hoechst 33342, anti-HA antibody, and anti-Sad1 antibody staining (3), which identified the DNA, Mcp4-3HA, and the SPB, respectively. The stage of meiosis of the cells was determined by the number of nuclei and the morphology of the SPB. Typical images taken at each meiotic stage are shown in Fig. 2A.

The fluorescence signal from Mcp4-3HA was not detected in vegetative growing cells, which further confirmed that Mcp4 expression is meiosis specific (Fig. 2A, top panels). During meiosis (Fig. 2A, remaining panels), the Mcp4-3HA signals first appeared faintly in the cytoplasm at the horsetail phase. At metaphase I, these signals accumulated in the cytoplasm as randomly scattered dots. At anaphase I, the signals became concentrated into many bright dots located around each of the two nuclei. At metaphase II, which is when the SPB duplicates and the two nuclei move to prepare for meiosis II, the Mcp4 dots remained around the nuclei. At early anaphase II, some dots were separate from the DNA (chromatin), as the chro-

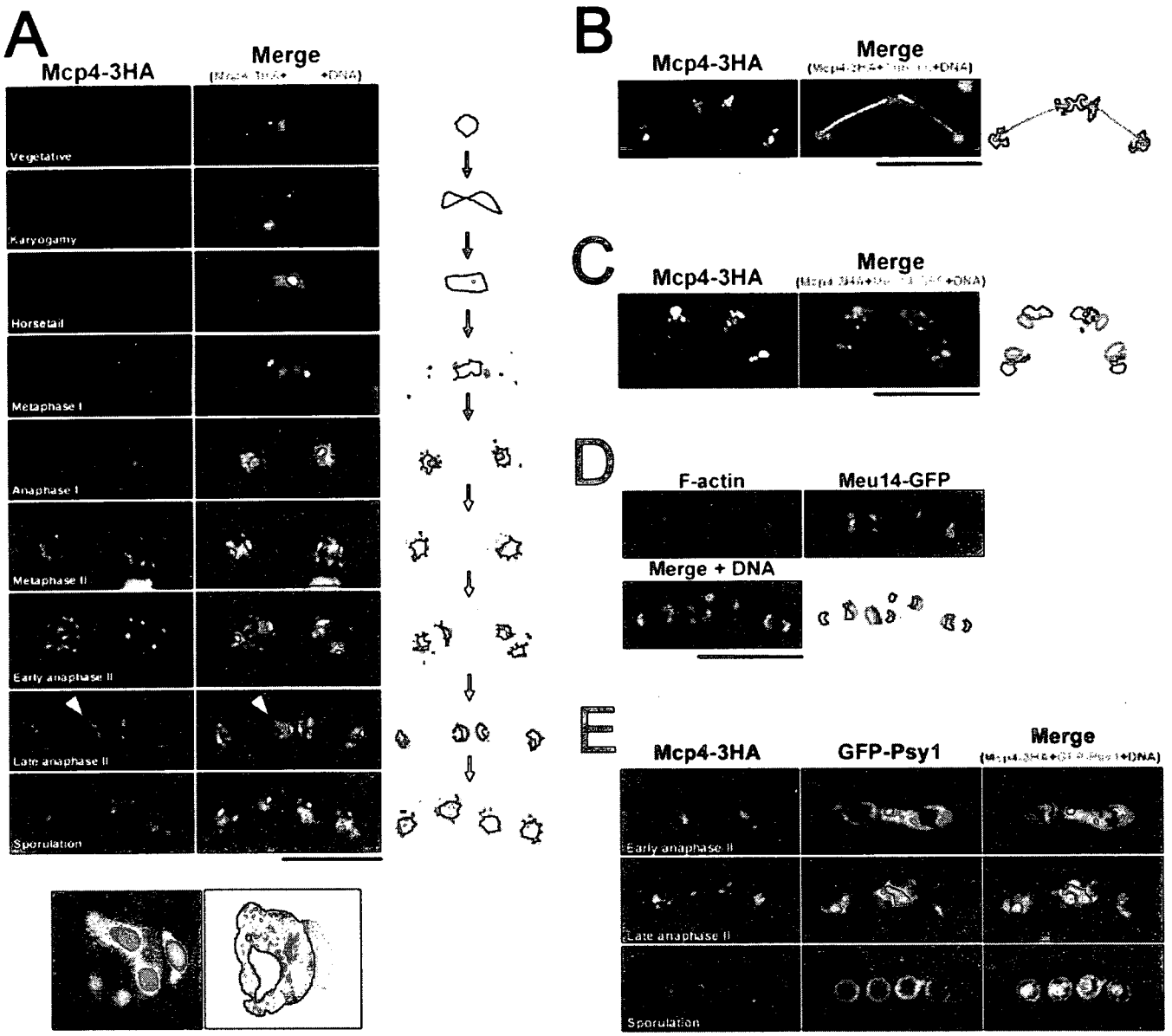

FIG. 2. Localization of Mcp4 during meiosis. The merged images are depicted schematically in the rightmost panels. (A) Comparison of the subcellular localizations of Mcp4, SPBs, and DNA during the vegetative cell cycle, meiosis, and sporulation. The homothallic haploid cell line AO64 (h^{90} *mcp4*$^{+}$-3ha) was cultured in EMM with appropriate supplements and either left in EMM or transferred to EMM-N to induce meiosis. The cells were fixed chemically at the vegetative growth phase or at different stages of meiosis and then stained with Hoechst 33342, anti-HA antibody, and anti-Sad1 antibody to detect the DNA (blue), Mcp4-3HA (red), and SPBs (green), respectively. The fluorescence microscopic images of these three cellular components are merged in the middle panels. The images indicated by arrowheads were enlarged and depicted schematically in the lower panels. (B) Comparison of the subcellular localizations of Mcp4-3HA, tubulin, and DNA. Chemically fixed AO64 cells at late anaphase II were stained with Hoechst 33342, anti-HA antibody, and anti-TAT1 antibody to visualize the DNA (blue), Mcp4-3HA (red), and tubulin (green), respectively. Mcp4 appears to aggregate close to both ends of the microtubules. (C) Comparison of the subcellular localizations of Mcp4-3HA, Meu14-GFP, and DNA. *meu14*$^{+}$-*gfp mcp4*$^{+}$-3ha cells (AO187) in anaphase II were chemically fixed and stained with Hoechst 33342 and anti-HA antibody. In the merged image, Meu14 is shown in green. The Mcp4 rings (red) are flanked by chromatin (blue) on one side and Meu14 rings on the other during late meiosis II. (D) Comparison of the subcellular localizations of F-actin and Meu14-GFP. AO185 cells were chemically fixed and stained with Hoechst 33342 and rhodamine-phalloidin to visualize the chromatin (blue) and F-actin (red), respectively. The F-actin occupies the space between the Meu14 (green) and Mcp4 rings shown in panel C. (E) Comparison of the subcellular localizations of Mcp4-3HA and GFP-Psy1. pREP81-*gfp-psy1*$^{+}$*mcp4*$^{+}$-3ha cells (AO194) in anaphase II and during sporulation were chemically fixed and stained with Hoechst 33342 and anti-HA antibody to visualize the chromatin (blue) and Mcp4 (red), respectively. GFP-Psy1 is shown in green. Mcp4 was localized at the leading edge of the FSM during anaphase II. Bars, 10 μm.

mosome shapes became deformed prior to nuclear division. This suggests that Mcp4 encircles the nuclear membrane but not the chromatin during anaphase I and metaphase II. At late anaphase II, the Mcp4 dots appeared to form a ring close to the perinucleus (see white arrowheads); the SPB is located on the opposite side of the nucleus. Thus, the Mcp4 ring and the SPB effectively sandwich the nucleus at late anaphase II. The Mcp4 ring is probably at the leading edge of the FSM. Upon

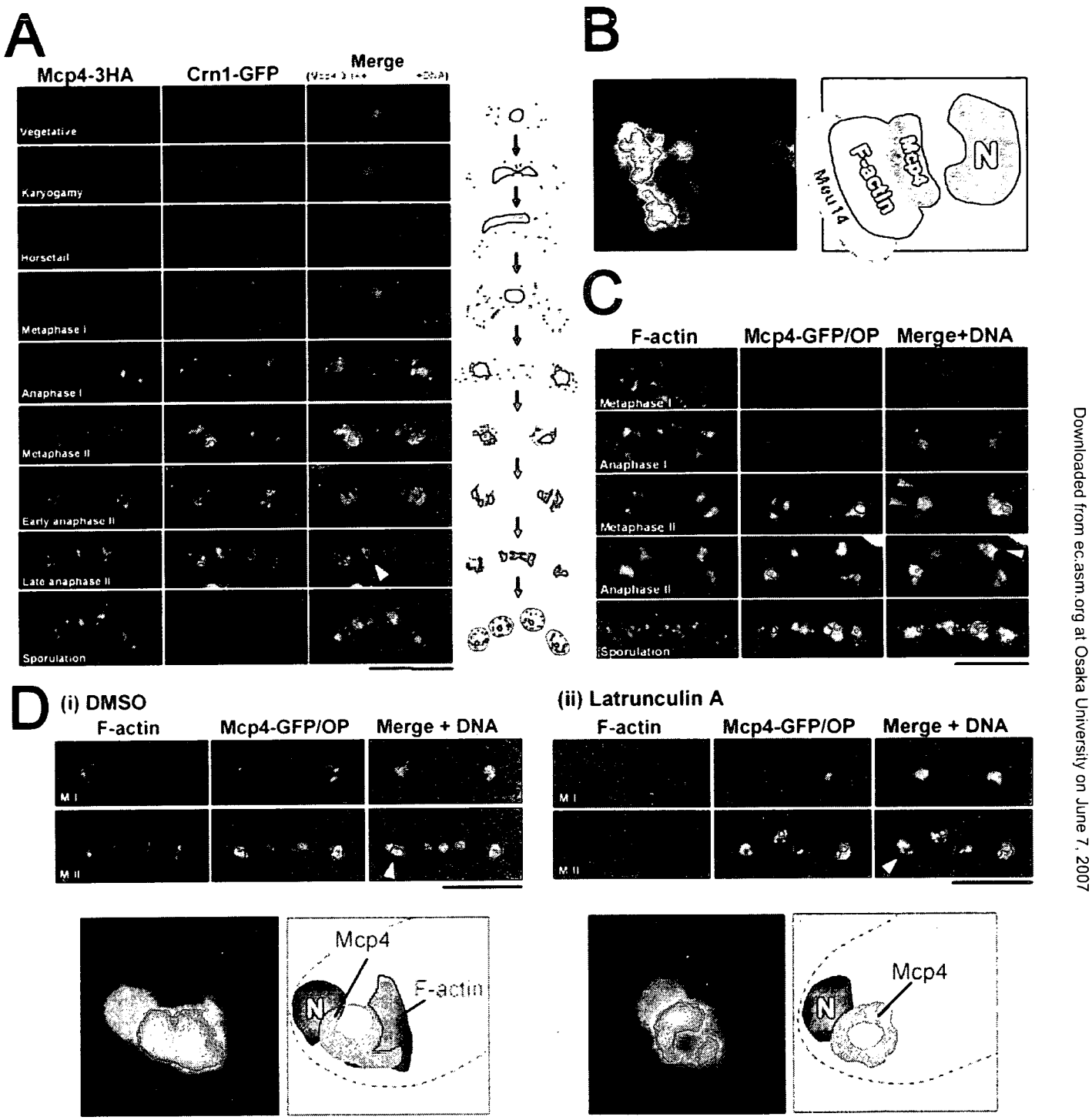

FIG. 3. Mcp4-GFP localizes side by side with F-actin during meiosis. (A) Microscopic analysis of Mcp4 and F-actin localization during meiosis. The homothallic haploid strain AO192 (h^{90} *mcp4*$^{+}$-3ha *crn1*$^{+}$-*gfp*), which expresses Crn1-GFP, was induced to enter meiosis, after which the cells were chemically fixed and stained with Hoechst 33342 and anti-HA antibody to detect DNA (blue) and Mcp4-3HA (red), respectively. Crn1-GFP, which marks the F-actin complex, was visualized directly through its GFP-derived fluorescence. The merged images are shown schematically in the rightmost panels. (B) Enlarged view (left) and its schematic depiction (right) of the merged image at late anaphase II indicated by the white arrowhead in panel A. The localization of Meu14 that was revealed in Fig. 2C and D is also shown. (C) Microscopic analysis of the meiotic localization patterns of F-actin and ectopically expressed Mcp4-GFP. The homothallic haploid strain AO00, which bears the *mcp4*$^{+}$-*gfp* plasmid and expresses Mcp4-GFP under the control of the *nmt41* promoter, was cultured in EMM containing 1 μg/ml thiamine with supplements and then transferred to EMM without thiamine to induce the expression of Mcp4-GFP. Subsequently, 10 h after the first medium replacement, the cells were transferred to fresh EMM-N without thiamine to induce meiosis. Cells at various stages of meiosis were chemically fixed and stained with Hoechst 33342 and 4 μM rhodamine-phalloidin to visualize the DNA (blue) and F-actin (red), respectively. Mcp4-GFP is shown in green. The merged images are shown in the rightmost panels. (D) Mcp4-GFP localization is independent of F-actin polymerization. *mcp4*Δ cells were transformed with

sporulation, the Mcp4 dots again loosely surrounded the nucleus. We confirmed that these cytoplasmic dots were not derived from the antibody background (see http://www.biken.osaka-u.ac.jp/lab/molgenet/Supplementary_data_EC.pdf). To confirm whether Mcp4 localizes at the leading edge of FSM, we examined the subcellular localization of Mcp4 with an FSM marker, GFP-Psy1. Indeed, Mcp4-3HA signals were detected at the leading edge of GFP-Psy1 signals, or the FSM (Fig. 2E).

To confirm this subcellular distribution of Mcp4 during meiosis, we immunostained tubulin in meiotic AO64 cells with the TAT1 antibody as well as visualizing Mcp4-3HA. This revealed that the Mcp4 dots accumulated at the junctions between the chromatin and tubulin at late anaphase II (Fig. 2B) (see http://www.biken.osaka-u.ac.jp/lab/molgenet/Supplementary_data_EC.pdf). We also compared the subcellular localization of Mcp4 with that of Meu14, which also forms a ring at the leading edge of the FSM (18). We found that Mcp4 is sandwiched between the nuclear chromatin and Meu14-GFP at late anaphase II (Fig. 2C). Notably, the late anaphase II image in Fig. 2C revealed a space between Mcp4 and Meu14. When the F-actin in cells carrying Meu14-GFP was stained with rhodamine-phalloidin in late anaphase II, it was found that this space was occupied by F-actin (Fig. 2D).

The detection of Mcp4 in the vicinity of the nucleus at metaphase II suggested that Mcp4 may localize in association with the nuclear membrane. Thus, we examined if Mcp4-3HA colocalizes with Cut15-GFP, which is known to exist in the nuclear membrane (12). We found that the two proteins displayed distinct localizations (see http://www.biken.osaka-u.ac.jp/lab/molgenet/Supplementary_data_EC.pdf), which indicates that the association of Mcp4 with the nuclear membrane, if any, is very weak. We also examined if Mcp4-3HA colocalizes with a septin homolog, Spn6-GFP, because the localization of budding yeast septin, an essential factor for sporulation, resembles that of Mcp4 (10). However, their localizations were different at both metaphase I and metaphase II (see http://www.biken.osaka-u.ac.jp/lab/molgenet/Supplementary_data_EC.pdf).

Mcp4-GFP localizes in the vicinity of F-actin. Since the subcellular localization of Mcp4 partially resembled that of F-actin (20), we examined whether Mcp4 colocalizes with F-actin during meiosis. For this purpose, we crossed the *mcp4*$^+$-3ha strain with FY13596 to generate a strain that expresses both Mcp4-HA and the coronin homologue Crn1 (5), which was tagged with GFP at its C terminus (Table 1). Crn1 forms a complex with F-actin, and Crn1-GFP has been used previously to visualize F-actin in vivo (19). As shown in Fig. 3A, while both Mcp4-3HA and F-actin appeared as cytoplasmic dots at metaphase I and anaphase I, very few of the dots colocalized. Moreover, at anaphase I, when some of the Mcp4-3HA dots started to accumulate around the nuclear membrane, Crn1-GFP (F-actin) did not show similar perinuclear accumulation; instead, its dots remained scattered in the cytoplasm. It was notable that even random colocalization was rarely detected. This suggests that F-actin and Mcp4 may actually avoid each other. At metaphase II, when most Mcp4-3HA signals maintained a loose perinuclear localization, the Crn1-GFP signals started to accumulate around the nucleus; the GFP signals were distributed next to the Mcp4-3HA signals rather than overlapping them. At early anaphase II, Mcp4-3HA localized to one side of the nucleus and became flanked on its other side by Crn1-GFP. By late anaphase II, this sandwiched situation became more apparent (Fig. 3A, white arrowhead). An enlarged view and schematic rendition of this image (Fig. 3B) clearly show that Mcp4-3HA localizes between the nucleus and Crn1-GFP at anaphase II. The data shown in Fig. 2 suggest that the F-actin is sandwiched in turn by Mcp4 and Meu14 (shown schematically in Fig. 3B). At the end of meiosis, both the Mcp4-3HA and Crn1-GFP signals were observed as scattered but nonoverlapping dots around the spore nuclei.

To confirm these subcellular localizations of Mcp4 and F-actin, we initially prepared strain AO56, which expresses Mcp4 tagged at its C terminus with GFP from the native *mcp4*$^+$ promoter. However, we could not observe a fluorescence signal due to little expression of the fusion protein. Thus, we next prepared strain AO00, which carries a plasmid expressing Mcp4-GFP from the *nmt41* promoter. This allowed us to visualize the fluorescent signal of Mcp4-GFP under a fluorescence microscope. These cells were induced to enter meiosis, after which they were fixed and stained for F-actin. As shown in Fig. 3C, the F-actin signals behaved very similarly to the Crn1-GFP signals shown in Fig. 3A. Briefly, at metaphase I and anaphase I, Mcp4-GFP and F-actin both occurred as nonoverlapping cytoplasmic dots, while at metaphase II, Mcp4-GFP was sandwiched by the nucleus on one side and F-actin on the other (red arrowheads). This sandwiching of Mcp4 became more apparent at anaphase II (white arrowhead). After sporulation, Mcp4-GFP and F-actin again appeared as nonoverlapping dots located loosely around the spore nuclei.

To investigate whether this subcellular localization of Mcp4 is dependent on the proper localization of F-actin, we treated AO00 with latrunculin A, which depolymerizes F-actin (8). Since polymerization of F-actin is required for normal spore formation, the addition of latrunculin A (50 μM) to the medium inhibits meiotic progression and causes abnormal spore formation (20). When Mcp4-GFP was observed in the absence (Fig. 3D, panel i) or presence (Fig. 3D, panel ii) of latrunculin A, Mcp4 rings were observed in the cells without rhodamine-phalloidin signals from polymerized F-actin (Fig. 3D, panel ii). However, localization of Mcp4-GFP was aberrant in the cells during the process of abnormal spore formation, which was caused by the addition of latrunculin A (data not shown). Thus, to minimize the effect of sporulation, we performed a pulse-chase experiment in which we added a high concentration of latrunculin A (200 μM) to the cells (AO192) at metaphase I or metaphase II and then chemically

the Mcp4-GFP-expressing construct pRGT41-*mcp4*$^+$, thus generating the AO189 strain. These cells were cultured in EMM containing 1 μg/ml thiamine with supplements and then transferred to EMM without thiamine to induce Mcp4-GFP expression. Subsequently, 10 h after the first medium change, the cells were transferred to fresh EMM-N without thiamine to induce meiosis and incubated for another 10 h. Two hours after the addition of dimethyl sulfoxide solvent (DMSO) (i) or 50 μM latrunculin A in dimethyl sulfoxide (ii), the cells were chemically fixed and stained with rhodamine-phalloidin. Bars, 10 μm. The images indicated with arrowheads were enlarged and depicted schematically in the lower panels.

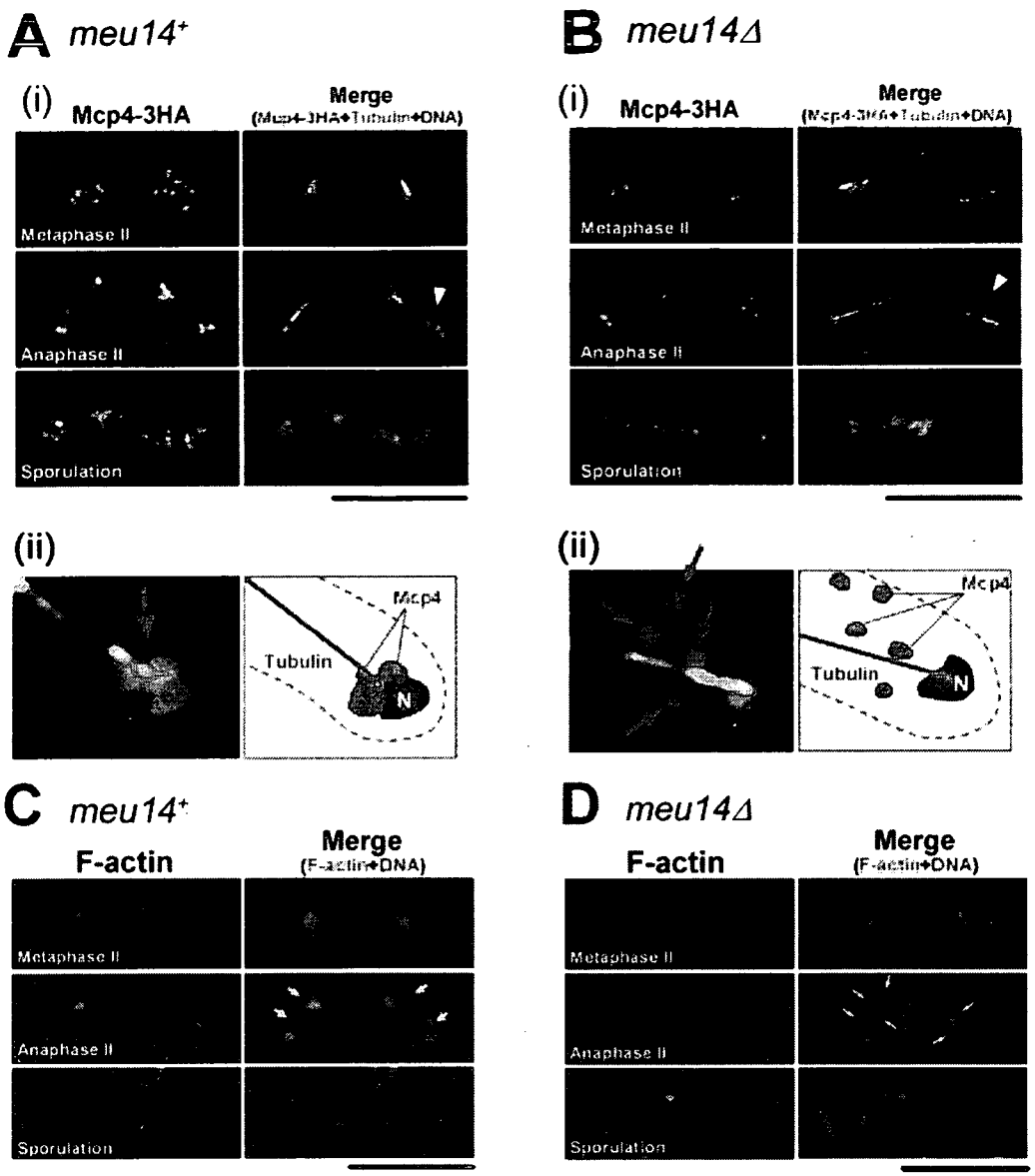

FIG. 4. Accurate positioning of Mcp4 at anaphase II depends on proper FSM formation. (A and B) Microscopic analysis of Mcp4-3HA localization in *meu14*$^+$ (A) and *meu14*Δ (B) cells during meiosis. The homothallic haploid strains AO185 (h^{90} *meu14*Δ *mcp4*$^+$-3ha) and AO64 (h^{90} *mcp4*$^+$-3ha) were cultured in EMM with appropriate supplements and then transferred to EMM-N to induce meiosis. After 10 h of incubation, the cells were chemically fixed and stained at different stages of meiosis with Hoechst 33342, the anti-HA antibody, and the anti-TAT1 antibody to detect the DNA (blue), Mcp4-3HA (red), and tubulin (green), respectively. (i) Typical images at metaphase II, anaphase II, and sporulation. The images are merged in the right panels. (ii) Enlarged views (left) of the cells at anaphase II denoted by white arrowheads in panels i and their schematic renditions (right). The red arrows indicate the Mcp4-3HA dots. (C and D) Typical images of F-actin in *meu14*$^+$ (AO64) (C) and *meu14*Δ (AO185) (D) cells at metaphase II, anaphase II, and sporulation. F-actin and DNA were stained with rhodamine-phalloidin (red) and Hoechst 33342 (blue), respectively. The yellow arrows indicate the aggregated F-actin patches. Bars, 10 μm.

fixed them after 1 h of incubation; this caused depolymerization of F-actin, but no spore formation occurred at this stage of meiosis. We found that Mcp4-3HA localized similarly in either the absence or presence of latrunculin A, even in the cells without fluorescent signals from Crn1-GFP (see http://www.biken.osaka-u.ac.jp/lab/molgenet/Supplementary_data_EC.pdf). These results indicate that formation of the Mcp4 ring is independent of F-actin polymerization.

Accurate positioning of Mcp4 at anaphase II depends on proper FSM formation. The subcellular localization pattern of Mcp4-3HA and Mcp4-GFP during meiosis suggested that Mcp4 plays a role in the proper positioning of the FSM. We previously reported that Meu14 plays an essential role in the formation of the FSM by localizing at its leading edge (18). Thus, we examined the subcellular localization of Mcp4-GFP in *meu14*Δ cells. Mcp4-3HA behaved normally at metaphase I (randomly scattered dots in the cytoplasm) as well as at anaphase I and metaphase II (perinuclear accumulation) (Fig. 2A and 4A and B, top panels; data not shown). At anaphase II, however, Mcp4-GFP did not accumulate near the junction

points of tubulin and the nuclei (Fig. 4B). Instead, as demonstrated by the enlarged views shown in Fig. 4A, panel ii, and B, panel ii (arrows), many of the Mcp4-GFP signals were randomly scattered away from the perinucleus.

We also examined the subcellular localization of F-actin during meiosis II in *meu14*Δ cells. We found that F-actin polymerization occurred normally in *meu14*Δ cells, since F-actin signals were detected (Fig. 4C and D). However, the positioning of F-actin during anaphase II was abnormal in these cells, as F-actin occurred as scattered dots in the cytoplasm away from the nucleus (Fig. 4C and D, orange arrows). Thus, Meu14 is required for the proper localization of both Mcp4 and F-actin during anaphase II.

Mcp4 is required for the proper alignment of F-actin at the FSM. To examine the meiotic role of Mcp4 in more detail, we constructed a null mutant lacking the *mcp4*$^+$ gene (*mcp4*Δ). We first investigated whether Mcp4 is required for the development of the FSM by visualizing GFP-Psy1 in *mcp4*Δ cells. During meiosis II, Psy1 translocates from the plasma membrane to the nascent FSM (15). Thus, monitoring the movement of GFP-Psy1 allows us to visualize the process of FSM formation. Time-lapse observation of GFP-Psy1 in live *mcp4*Δ cells under a fluorescence microscope revealed a normal subcellular distribution and movement of GFP-Psy1 (data not shown). Moreover, *mcp4*Δ cells developed FSMs and formed four nucleated prespores as efficiently as did wild-type cells (data not shown).

Next, to investigate how F-actin behaves during FSM formation in *mcp4*Δ cells, we compared the subcellular localizations of F-actin and GFP-Psy1 under a fluorescence microscope. At metaphase II, we found that F-actin behaved normally (Fig. 5A and B, white arrowheads in upper panels). However, at anaphase II, when the FSM was almost closed (as visualized by GFP-Psy1), the F-actin signals formed a balloon shape in *mcp4*Δ cells rather than a dumbbell shape (Fig. 5A, panel i, and B, panel i, red arrowheads in the bottom panels). The disparate F-actin signals are shown by the enlarged pictures (Fig. 5A, panel ii, and B, panel ii, red arrows and arrowhead) and their schematic renditions (right panels). Bar graphs summarizing the proportion of cells harboring zero to four dumbbell or balloon shapes clearly indicate that almost all *mcp4*Δ cells have aberrant balloon-shaped F-actin at anaphase II (Fig. 5C). Thus, Mcp4 helps to regulate the positioning of F-actin at the aperture of the closing FSM.

We also examined the meiotic progression, spore morphology, and spore viability of *mcp4*Δ cells and found that all were almost completely normal (see http://www.biken.osaka-u.ac.jp/lab/molgenet/Supplementary_data_EC.pdf). Examination of the sensitivity of *mcp4*Δ spores to ethanol, Glusulase, high temperature, high pH (6.8), low pH (3.5), and osmotic stress imposed by high concentrations of salts, such as KCl or $CaCl_2$, also revealed no abnormalities. However, we found that *mcp4*Δ spores were sensitive to high sodium salt concentrations, i.e., *mcp4*Δ spores grew slower than *mcp4*$^+$ spores when returned to the nitrogen-rich plate (Fig. 5D) and the spore viability was slightly lowered in the presence of 175 mM NaCl (Fig. 5E). Under microscopy, the population of spores that failed to form colonies was increased for the *mcp4*Δ strain compared to the *mcp4*$^+$ strain in the presence of a high NaCl concentration, and most of these spores appeared to be germinated abnormally (Fig. 5F). These mild phenotypes of the *mcp4*Δ cells were probably due to the abnormal regulation of FSM formation, as described above, and the resulting weaker cell wall integrity. We also measured the meiotic recombination rates of *mcp4*Δ cells and found that they were only slightly depressed (see http://www.biken.osaka-u.ac.jp/lab/molgenet/Supplementary_data_EC.pdf).

The C-terminal domain of Mcp4 harboring the coiled-coil motif participates in proper localization of Mcp4. Next, to investigate the role that the coiled-coil domain of Mcp4 plays in its meiotic function, we examined the subcellular localization of Mcp4 lacking the C-terminal coiled-coil domain (Mcp4ΔC) (Fig. 6A). We first examined how ectopically expressed intact and truncated Mcp4 proteins localize in mitotic cells stained with the fluorescent styryl dye FM4-64, which stains the Golgi/endosome membranes after 5 min of uptake and then the vacuole membrane 60 min later (2). In both Mcp4-GFP- and Mcp4ΔC-GFP-expressing cells, we did not find any GFP signals in the Golgi complex/endosome (Fig. 6C, panels i and ii, upper panels). The observation that Mcp4ΔC-GFP and Mcp4-GFP do not localize at stable Golgi/endosome structures was confirmed by the failure of these proteins to colocalize with cyan fluorescent protein (CFP)-labeled Rer1, an ER/Golgi complex shuttling protein (17, 24) (Fig. 6B). However, Mcp4ΔC-GFP (Fig. 6C, panel ii, lower panels) appeared to colocalize with the 60-minute FM4-64 signal in the vacuole, unlike the intact Mcp4 protein (Fig. 6C, panel i, lower panels). This is probably due to the highly hydrophobic nature of Mcp4ΔC-GFP.

Next, we examined the role that the coiled-coil domain of Mcp4 plays in meiosis. Since we could not detect the Mcp4-GFP signal by using the native promoter, as described above, we ectopically expressed the intact Mcp4-GFP or truncated Mcp4ΔC-GFP protein. Comparison of the fluorescence signals from GFP and FM4-64 revealed that Mcp4-GFP dots did not colocalize with FM4-64, which primarily stained the vacuole during meiosis (Fig. 6D, panel i). In contrast, the Mcp4ΔC-GFP signals did not occur as scattered dots, but rather, they aggregated into small rings that did not colocalize with FM4-64 signals but were localized in the vicinity of the vacuole (Fig. 6D, panel ii).

When we compared the localization patterns of the truncated Mcp4 protein and F-actin, we found that while intact Mcp4-GFP was sandwiched between the nucleus and F-actin (Fig. 6E, panel i, white arrowheads), Mcp4ΔC-GFP appeared to have lost its proper sandwiched distribution. Instead, it displayed a large ring-shaped structure (Fig. 6E, panel ii, white arrowheads). Nonetheless, we found that the sporulation of cells ectopically expressing Mcp4ΔC-GFP appeared to be almost normal (data not shown). Taken together, these results indicate that the C-terminal domain of Mcp4 harboring a coiled-coil motif is required for the proper localization of Mcp4.

DISCUSSION

Mcp4 is required for accurately positioning F-actin at anaphase II. In the present study, we characterized the function of the meiosis-specific *mcp4*$^+$ gene, which is highly expressed during the meiotic cell cycle only. We found by Northern blot and Western blot analyses that the expression of the *mcp4*$^+$

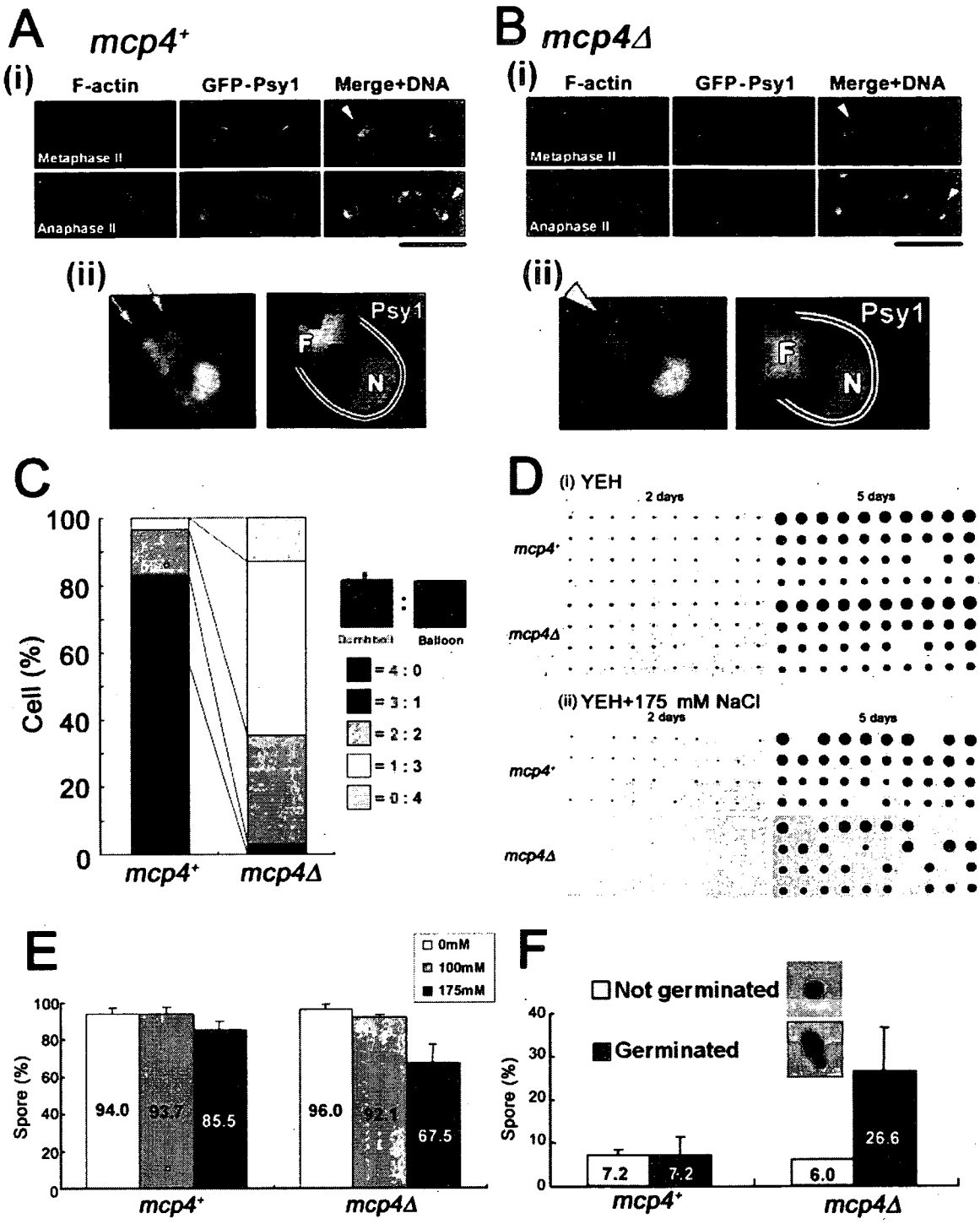

FIG. 5. Phenotypes of *mcp4*Δ cells during meiosis. (A and B) Mcp4 is required for proper formation of the F-actin structure at anaphase II. GFP-Psy1-expressing *mcp4*$^+$ (YN68) (A) and *mcp4*Δ (AO125) (B) strains were induced to enter meiosis by nitrogen starvation. After 10 h, the cells were chemically fixed and stained with rhodamine-phalloidin to detect F-actin. (i) Typical fluorescence microscope images at metaphase II and anaphase II. The images for F-actin (red), GFP-Psy1 (green), and DNA (blue) are merged in the right panels. (ii) Enlarged views of the images indicated by the arrowheads in panels i and their schematic renditions. F-actin forms a dumbbell shape in *mcp4*$^+$ cells (red arrows in panel A, part ii) but a balloon shape in *mcp4*Δ cells (red arrowhead in panel B, part ii). Bars, 10 μm. (C) Quantitative analysis of the cell populations harboring zero to four dumbbell or balloon shapes in the *mcp4*$^+$ or *mcp4*Δ strain at anaphase II. The bar graphs were drawn by counting the F-actin shapes in 30 *mcp4*$^+$ and 31 *mcp4*Δ cells. (D to F) *mcp4*Δ spores are more salt sensitive than *mcp4*$^+$ spores. *mcp4*$^+$ (YN68) and *mcp4*Δ (AO125) spores were separated by a manipulator onto YEH agar plates, with or without 0.1 M or 0.17 M NaCl. The plates were incubated at 30°C for 5 days. (D) Sizes of colonies of *mcp4*Δ spores after 2 or 5 days on a YEH plate in the absence (0 mM) or presence (175 mM) of NaCl. (E) Viability of *mcp4*Δ spores under high NaCl conditions. Spores of *mcp4*$^+$ and *mcp4*Δ cells were dissected by a micromanipulator. The data shown are the average values for at least three independent assays (at least 80 spores were dissected per assay). The standard deviations are indicated by the error bars. (F) Quantitative analysis of spore populations that could not make colonies when returned to the YEH plate under high sodium salt conditions. Typical images of the germinated spores for *mcp4*$^+$ and *mcp4*Δ strains are shown in the insets. The data shown are the average values for at least three independent assays. At least 8 or 22 spores were dissected per assay for the *mcp4*$^+$ or *mcp4*Δ strain, respectively. The standard deviations are indicated by the error bars.

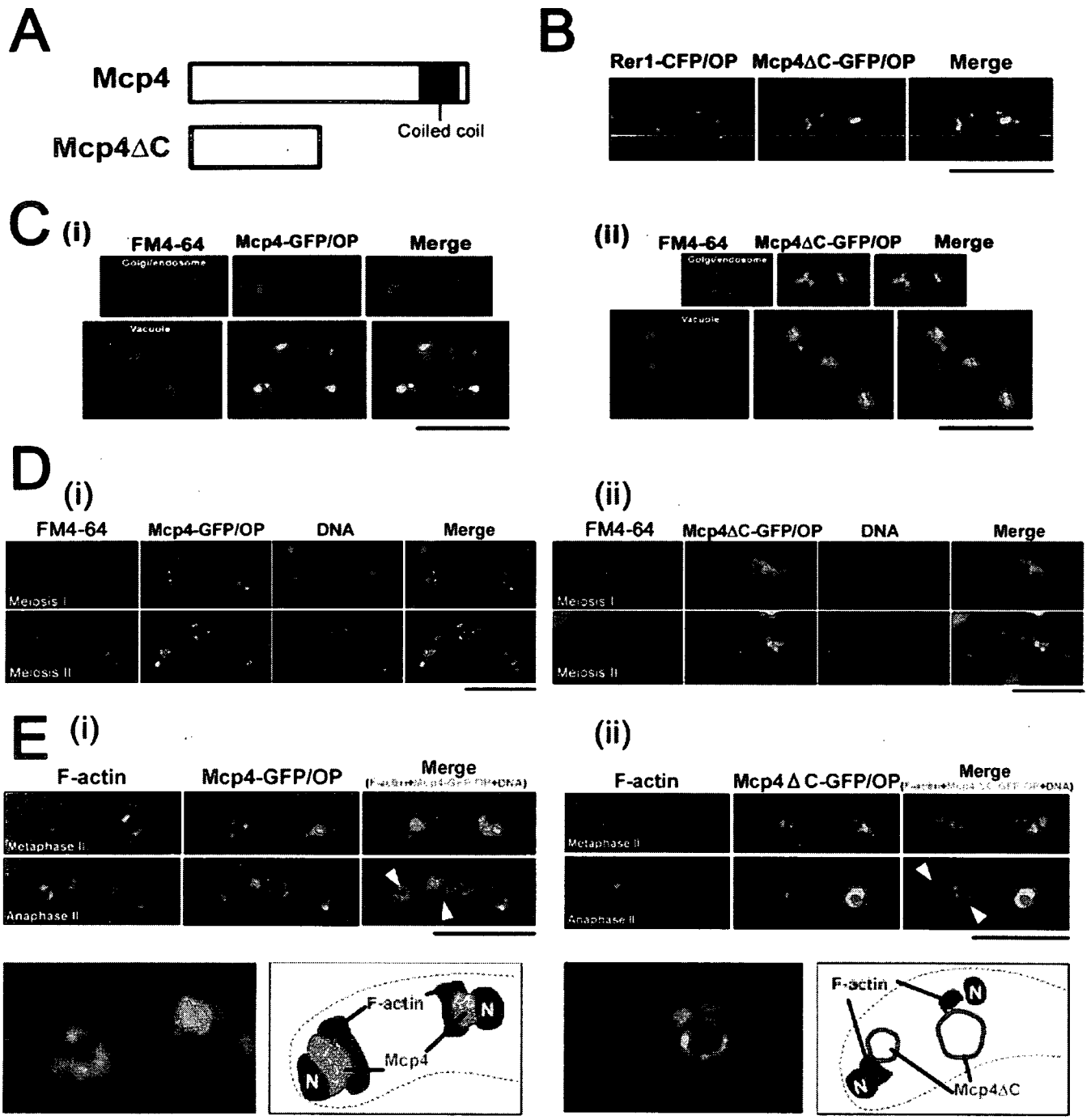

FIG. 6. The C-terminal coiled-coil domain of Mcp4 is required for proper localization of this protein during meiosis. (A) Schematic depiction of Mcp4 and Mcp4ΔC. The coiled-coil motif is indicated by the black box. (B) Comparison of the localization patterns in mitotic cells of ectopically expressed Mcp4ΔC-GFP and CFP-labeled Rer1. Rer1 is an ER/Golgi complex shuttling protein (17, 24). Mitotic AO168 (*mcp4ΔC-GFP rer1*$^+$*-cfp*) cells were cultured in EMM without thiamine. The merged images are shown in the rightmost panel. (C to E) Comparison of the localization patterns of ectopically expressed Mcp4-GFP (i) and Mcp4ΔC-GFP (ii) in mitotic (C) and meiotic (D and E) pREP41 (*mcp4*$^+$*-gfp* or *mcp4ΔC-gfp*) cells. (C) The cells were cultured in EMM without thiamine and stained with FM4-64 (red). This allowed us to visualize the Golgi complex/endosome 5 min after uptake and then the vacuole 60 min later. (D and E) The cells were cultured in EMM containing 1 μg/ml thiamine with supplements and then transferred to EMM without thiamine to induce Mcp4-GFP expression. Subsequently, 10 h after the first medium exchange, the cells were transferred to fresh EMM-N without thiamine to induce meiosis. After incubation for 10 h, live cells were observed under a fluorescence microscope in the presence of FM4-64 (red) to visualize the localization of the Golgi complex/endosome and the vacuole (D), or the cells were chemically fixed and stained with rhodamine-phalloidin (red) to detect F-actin (E). The green and blue signals are from Mcp4ΔC-GFP and Hoechst 33342-stained DNA, respectively. The merged images are shown in the rightmost panels. The images denoted by the white arrowheads in panel E are enlarged and depicted schematically in the bottom panels. Bars, 10 μm.